Capturing Multi-Scale Dynamics of Aortic Valve Calcification With a Coupled Fluid–Structure and Systems Biology Model

Michael Quan[1], Tianyou Xie[1], Leonard A. Harris[2,3], and Haoxiang Luo*[1]

[1] *Department of Mechanical Engineering, Vanderbilt University, 2201 West End Avenue, Nashville, TN 37235, USA*

[2] *Department of Biomedical Engineering, University of Arkansas, Fayetteville, AR 72701, USA*

[3] *Cancer Biology Program, Winthrop P. Rockefeller Cancer Institute, University of Arkansas for Medical Sciences, Little Rock, AR 72205, USA*

November 28, 2025

Abstract

Calcific aortic valve disease (CAVD) arises from coupled interactions between blood flow, tissue mechanics, and cellular signaling. Hemodynamic forces influence endothelial and interstitial cell behavior, while the resulting tissue remodeling alters valve motion and flow patterns. Capturing this two-way feedback requires models that integrate fluid–structure mechanics with biochemical regulation, yet such multiscale coupling remains technically challenging. Previous computational models have focused on isolated aspects of the disease: fluid–structure interaction (FSI) simulations reproduce valve deformation and flow, and systems biology (SB) models describe molecular signaling that drives fibrosis and calcification. However, without coupling, these approaches cannot predict how mechanical dysfunction initiates biochemical remodeling or how biochemical changes feed back on mechanics. Here, we present a multi-physics computational framework that couples three-dimensional FSI simulations of aortic valve dynamics with a mechanistic SB model of calcification signaling. The FSI module resolves pulsatile blood flow and leaflet deformation, yielding local wall shear stresses and tissue strains throughout the cardiac cycle. These mechanical quantities are used as inputs to the SB module, which represents key biochemical pathways governing inflammation, TGF-β/SMAD signaling, and nitric-oxide (NO)–mediated inhibition within valvular cells. Simulations predict long-term calcification trajectories for valves of varying thickness, showing that fibrosis-induced stiffening lowers shear stress, reduces NO synthesis, and enhances TGF-β activation, thereby accelerating calcification. The framework is modular and extensible, allowing future incorporation of additional pathways, as well as implementation of full two-way coupling between the FSI and SB models. By integrating physics-based hemodynamics with systems-level biochemistry, this study provides a proof-of-principle demonstration of a next-generation, multi-scale modeling platform for studying cardiovascular disease that unites blood flow dynamics and biochemical signaling.

1 Introduction

The aortic valve is a dynamic, load-bearing structure that experiences substantial mechanical stress with every cardiac cycle. Over time, this stress contributes to pathological remodeling and calcification of the valve leaflets due to a complex interplay between hemodynamic forces, cellular signaling, and tissue remodeling.[1,2]

*Corresponding author: haoxiang.luo@vanderbilt.edu

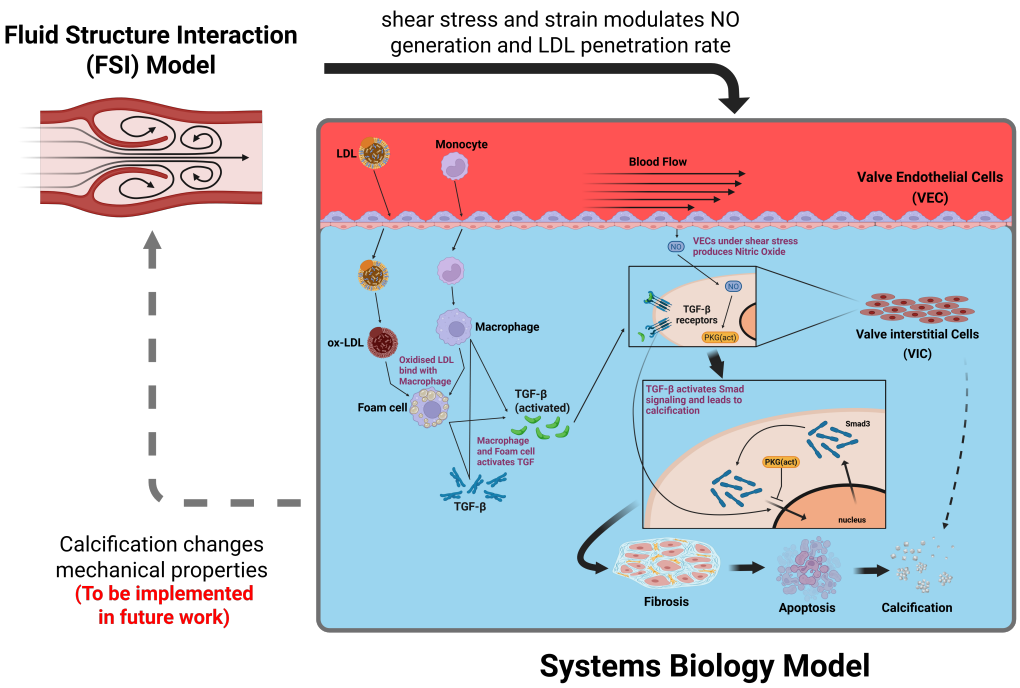

Figure 1: ***Schematic of the coupled FSI–SB framework to model mechanobiological drivers of CAVD progression.*** *The 3D fluid structure interaction (FSI) model (left) computes flow-induced shear stress and tissue strain on the aortic valve leaflets, which serve as inputs to the systems biology (SB) model (right). These mechanical signals regulate endothelial NO production, LDL penetration, inflammatory activation, and TGF-β–dependent SMAD signaling within valve endothelial cells (VECs) and valve interstitial cells (VICs). The SB model integrates these pathways to simulate downstream fibrotic, apoptotic, and calcific processes. In the current implementation, information flows from the FSI model to the SB model. Future work will implement two-way coupling between the modules to account for how changes in the tissue material properties affect blood flow through the valve.*

Progressive calcification restricts valve opening, increases left ventricular afterload, and ultimately leads to aortic stenosis and heart failure. Despite the growing prevalence of calcific aortic valve disease (CAVD), no pharmacological therapies currently exist to halt or reverse its progression, and valve replacement remains the only effective treatment.[1,3] Mechanobiological studies have shown that CAVD is not a passive degenerative process but a dynamic, regulated sequence of events involving endothelial activation, inflammatory infiltration, and maladaptive remodeling of the extracellular matrix.[4,5] Hemodynamic forces are key determinants of disease initiation and progression: the aortic and ventricular surfaces of the valve experience distinct shear stress patterns that differentially regulate nitric oxide (NO) signaling and inflammation,[6,7] while altered mechanical strain promotes myofibroblast differentiation and calcific nodule formation.[8,9] These observations indicate that valve pathology emerges from the reciprocal interplay between blood flow, tissue mechanics, and cellular signaling. Capturing this reciprocity requires models that account for both the mechanical environment that acts on valve cells and the intracellular pathways that determine how those cells respond.

A substantial body of computational research has been devoted to modeling the mechanics and hemodynamics of the aortic valve. Three-dimensional fluid–structure interaction (FSI) simulations have been widely used to investigate the hemodynamics and mechanics of the native and prosthetic aortic valve, resolving complex flow structures, leaflet deformation, and wall shear stress (WSS).[10–17] These studies have clarified how valve geometry, stiffness, and flow conditions affect opening kinematics and stress distribution.[18–20] Independently, systems biology (SB) models have been developed to describe the biochemical networks and signaling pathways that regulate inflammation, fibrosis, and calcification.[21–24] Transforming growth factor-beta (TGF-β) and small mothers against decapentaplegic (SMAD) signaling are known to drive fibroblast activation and extracellular matrix production,[25–27] while endothelial NO and cyclic guanosine monophosphate (cGMP) signaling exert

protective, anti-fibrotic effects by suppressing SMAD3 activity.[28,29]

Although these mechanical and biochemical models have each contributed important insights into aortic valve calcification, they operate largely in isolation. Without coupling, they cannot capture the mechanochemical feedbacks by which mechanical dysfunction initiates molecular remodeling or how progressive fibrosis and calcification alter valve mechanics. Establishing this link is challenging because the underlying processes occur on vastly different spatial and temporal scales: valve motion and flow evolve over milliseconds, whereas biochemical signaling and tissue remodeling unfold over years. These challenges motivate the development of tractable, modular frameworks that can connect well-validated FSI solvers with mechanistic SB models to quantify mechanochemical feedback in CAVD. In this study, we present a coupled multi-physics computational framework that integrates three-dimensional FSI simulations of aortic valve dynamics with a mechanistic SB model of calcification signaling (Fig. 1). The FSI module resolves pulsatile blood flow and leaflet deformation using a sharp-interface immersed-boundary method,[16,17,30] yielding spatial and temporal distributions of WSS and tissue strain throughout the cardiac cycle. These mechanical quantities serve as inputs to the SB module, which we have developed in this work by combining three major processes: (1) activation of TGF-β and the inflammation pathway,[31,32] (2) SMAD-mediated signaling that drives fibroblastic differentiation and fibrosis,[33–35] and (3) endothelial NO synthesis and its inhibitory effect through the NO/cGMP/protein kinase G (PKG) pathway.[6,36,37] Simulation results of the coupled aortic valve calcification model reveal a self-reinforcing mechanochemical feedback: fibrosis-induced stiffening of the valve reduces WSS, decreases endothelial NO synthesis, and enhances TGF-β activation, thereby accelerating calcification. These findings highlight how mechanical dysfunction can amplify molecular remodeling, offering a mechanistic explanation for the rapid progression of fibrotic thickening and calcification observed in patients with CAVD.[27,38]

The multi-scale framework proposed in this work provides a foundation for exploring the coupled physical and biochemical processes that govern aortic valve remodeling and for developing predictive modeling approaches to cardiovascular disease. By linking physics-based hemodynamics with systems-level biochemistry, the framework enables dynamic simulation of how cellular signaling pathways respond to evolving mechanical environments over time. Although the present implementation employs an idealized valve geometry and the two-way coupling between the FSI and the SB module is yet to be fully implemented, these controlled simplifications allow for a computationally tractable, proof-of-principle demonstration of how hemodynamic inputs can drive biochemical remodeling *in silico*. The following sections describe the computational methodologies and model formulations used, present simulation results, and discuss the limitations, implications, and future extensions of this integrated computational approach.

2 Methods and Models

2.1 Computational FSI model of blood flow through the aortic valve

The 3D FSI model, adopted from previous work,[30] has been applied to computational modeling of the aortic valve extensively.[16,17] The approach incorporates a direct forcing, immersed-boundary solver for the flow, a finite element method (FEM) solver for the solid mechanics, and strong coupling between the solvers. The two solvers are parallelized through a message passing interface (MPI), so they run in parallel. At each time step, the solvers exchange data and repeat their own computation until overall convergence is achieved. Specifically, the flow solver sends the boundary load, including the pressure and shear stresses, to the solid solver, and the solid solver sends the boundary displacement and velocity of the solid body to the flow solver. Additional details of the model implementation can be found in Refs. 16 and 17.

This FSI framework is versatile and can handle complex and arbitrary geometries of solid bodies. It has previously been validated against several benchmark problems, including moving boundaries and deformable-structures with two-way interactions.[30,39] In the current study, we consider a simplified geometry of the aorta[17] (Fig. 2a), where the tricuspid valve is placed within the aortic sinus with a tri-lobed dilation. The leaflets are assumed to be symmetric and have a uniform thickness, h, which is chosen here to be 0.3, 0.5, or 0.75 mm. The aorta is modeled as a straight and rigid tube with length $L = 19$ cm and diameter $D = 2.24$ cm. At the inlet of the tube, a transient pressure load is applied to drive blood flow (Fig. 2b). The outlet pressure is kept at 0 kPa

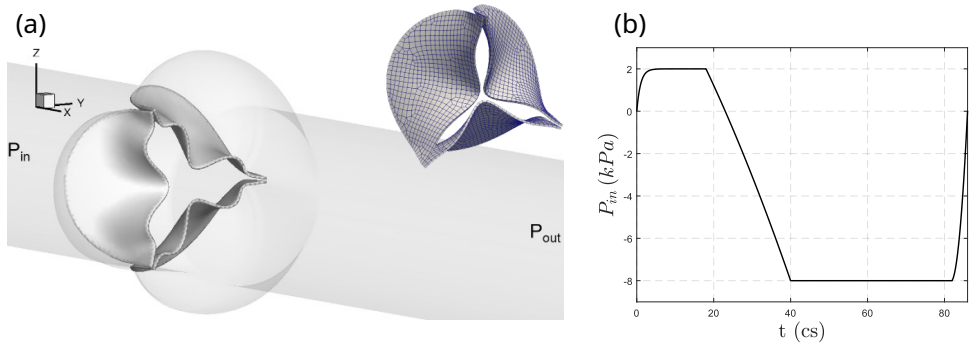

Figure 2: ***Idealized aortic valve geometry and loading conditions.*** *(a) Geometry and finite element discretization of a tri-leaflet aortic valve attached to a cylindrical tube with three outward-shaped lobes representing the aortic root. Shown are both the anatomical configuration of the valve within the lobed tube (left) and the corresponding FEM mesh used for solid mechanics in the FSI simulations (right). (b) Prescribed transvalvular pressure waveform applied across the valve during a single cardiac cycle, with positive pressure driving systolic opening and negative pressure driving diastolic closure.*

for all simulations. This setup provides physiologically consistent results, such as the opening area, volume flow rate, and opening and closing dynamics of the valve.[17]

Blood is assumed to be incompressible, governed by the viscous Navier-Stokes equations,

$$\rho\left(\frac{\partial v_i}{\partial t}+\frac{\partial v_i v_j}{\partial x_j}\right)=-\frac{\partial p}{\partial x_i}+\mu\frac{\partial^2 v_i}{\partial x_j \partial x_j} \tag{1}$$

$$\frac{\partial v_i}{\partial x_i}=0 \tag{2}$$

where ρ is blood density, v_i is fluid velocity, p is pressure, and μ is dynamic viscosity. Here, we set $\rho = 1$ g/cm^3 and $\mu = 0.005$ Pa·s. The leaflet tissue of the aortic valve is known to be both anisotropic and inhomogenous due to the alignment of the collagen and elastin fiber networks. For the purposes of this study, the hyperelastic Saint Venant-Kirchoff model[40] is used to represent the behavior of the leaflets. Previous works[17] have verified that under this model, simulated valves exhibit physiologically accurate valve opening/closing kinematics. The dynamics of leaflet deformation are governed by

$$\rho_s\frac{d^2u_i}{dt^2}+\eta_d\frac{du_i}{dt}=\frac{\partial\sigma_{ij}}{\partial x_j}, \tag{3}$$

where u_i is the deformation, ρ_s is the leaflet density, η_d is the damping coefficient, and σ_{ij} is the Cauchy stress tensor. Here, we set $\rho_s = 1$ g/cm^3 and η_d is chosen such that $h\eta_d = 1$ g/(cm^2· cs). Furthermore, to calculate σ_{ij}, the Young's modulus of the tissue $E = 2000$ kPa and Poisson's ratio $\nu = 0.4$.[15,19,41] A contact algorithm based on the penalty approach[16,17] is also applied at the leaflet surface to prevent leaflets from penetrating each other during the diastolic phase.

For spatial discretization, the aortic tube is divided into 20,735 triangle elements and 10,590 nodes, and the leaflets are divided into 1,617 20-node hexahedron elements (539 elements per leaflet; Fig. 2a). The flow domain is a $10.8 \times 4.4 \times 4.4$ cm rectangular box, discretized by a $400 \times 130 \times 130$ nonuniform Cartesian grid. No-slip and no-penetration boundary conditions are applied on the surface of the leaflets and the aortic wall. Simulations are run for the duration of one cardiac cycle, $T = 0.8$ s, with a flow solver timestep $\Delta t_{\text{flow}} = 4\times10^{-3}$ centi-seconds (cs) and solid solver timestep $\Delta t_{\text{solid}} = 5 \times 10^{-5}$ cs. Further, each Δt_{solid} consists of 80 substeps.

2.2 SB model of aortic calcification

To capture the biochemical processes that drive CAVD progression, we constructed an integrated SB model that combines three mechanistically distinct but tightly interconnected pathways: an inflammation module describing

LDL infiltration, oxidation, and immune activation; a TGF-β/SMAD signaling module governing fibroblastic differentiation and pro-calcific transcriptional activity; and an endothelial NO/cGMP/PKG module mediating shear-dependent inhibition of SMAD3. These sub-models, adapted from prior work and reformulated within a unified framework, enable dynamic simulation of how mechanical cues provided by the FSI model influence lipid transport, cytokine signaling, transcriptional regulation, and ultimately calcium deposition. The following subsections summarize the structure and key features of each module and describe how they are coupled into a single mechanistic model of aortic valve calcification.

2.2.1 Inflammation pathway

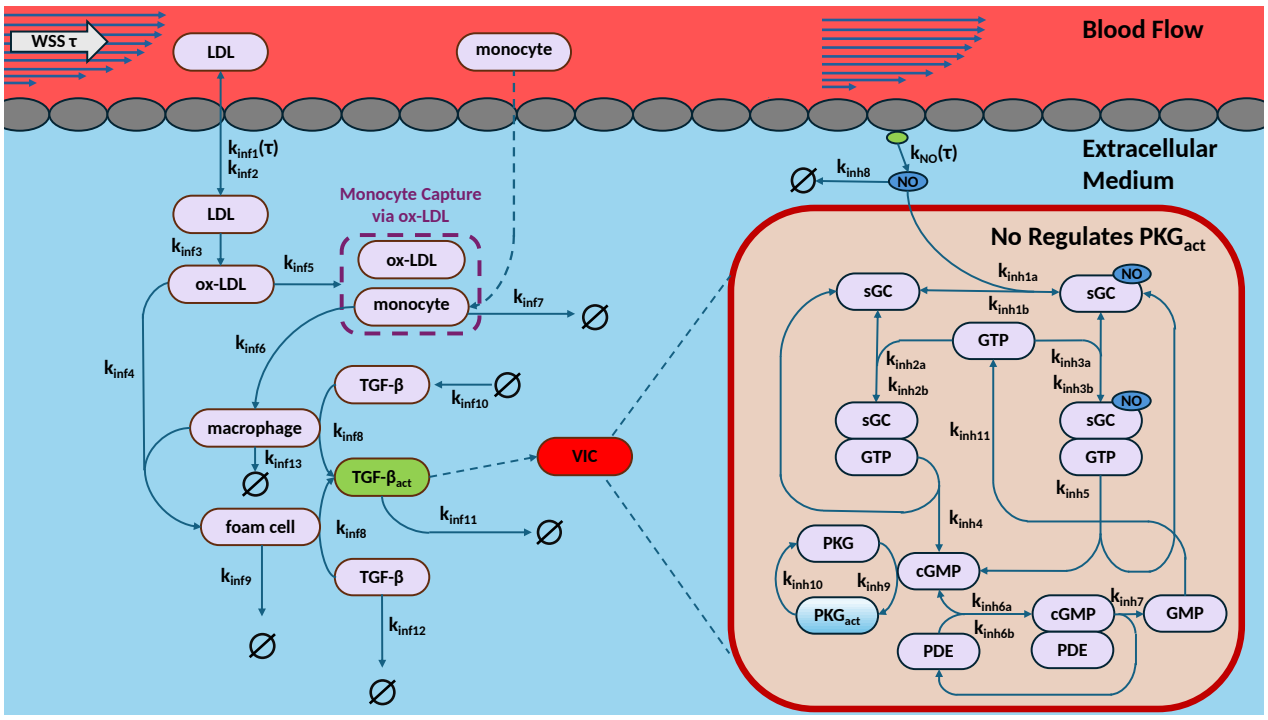

Figure 3: ***Mechanistic models of inflammation and NO regulation in aortic valve calcification.*** *In the inflammation model (left), low WSS increases subendothelial LDL penetration and oxidation, promoting monocyte recruitment, macrophage and foam cell formation, and activation of latent TGF-β. Active TGF-β serves as the upstream input to VIC SMAD signaling. The NO pathway (right) describes WSS-dependent NO production via eNOS, subsequent sGC-mediated cGMP generation, and PKG activation, which inhibits pro-calcific SMAD3 signaling. Arrows denote biochemical reactions; dashed arrows represent transport or recruitment processes.*

Since fibroblastic differentiation and subsequent apoptosis of valve interstitial cells (VICs) are a predominant contribution to the formation of calcific nodules on aortic valve leaflets,[4] the SB inflammation model, adapted from Arzani et al.,[21] focuses on calcification mediated through fibroblastic pathways (Fig. 3). The process begins with the subendothelial infiltration of low-density lipoproteins (LDL) into the valve tissue, where LDL undergoes oxidation. Oxidized LDL (oxLDL) promotes the recruitment of circulating monocytes from the bloodstream, which differentiate into macrophages within the valve's microenvironment.[1] Macrophages can further interact with oxLDL to form foam cells, which are lipid-laden cells implicated in chronic inflammation and commonly observed in atherosclerotic plaques. This process is modeled as

$$[oxLDL] + [Macrophage] \xrightarrow{k_{\mathrm{inf4}}} [Foam\ \ Cell] \tag{4}$$

Accumulation of immune cells within the tissue, particularly macrophages and foam cells, leads to the activation of latent TGF-β, initially secreted by macrophages in an inactive form.[42,43] These activation processes are modeled as

$$[Macrophage] + [TGF\beta] \xrightarrow{k_{\mathrm{inf8}}} [Macrophage] + [TGF\beta_{\mathrm{act}}] \tag{5}$$

$$[Foam\ Cell] + [TGF\beta] \xrightarrow{k_{\text{inf8}}} [Foam\ Cell] + [TGF\beta_{\text{act}}] \tag{6}$$

Once activated, TGF-β binds to receptors on the surface of VICs, initiating the process of myofibroblastic differentiation.[42] This transition promotes ECM remodeling, VIC apoptosis, and ultimately the formation of calcific nodules. Note that the Arzani et al.[21] inflammation model does not include SMAD signaling, with calcification directly dependent on TGF-β. Macrophages are also assumed to grow without bound. Here, we remedy this by including macrophage cell death, modeled as $[Macrophage] \xrightarrow{\text{k}_{\text{inf13}}} \emptyset$.

2.2.2 SMAD signaling

SMAD signaling is initiated within VICs upon binding of activated TGF-β to both TGF-β receptor types I and II (TGFβRI and TGFβRII) on the VIC surface (Fig. 4). We model TGF-β ligand-receptor binding by

$$[TGF\beta_{\text{act}}] + [R2]_s \underset{k_{\text{sma1b}}}{\overset{k_{\text{sma1a}}}{\rightleftharpoons}} [R2\text{-}TGF\beta_{\text{act}}]_s \tag{7}$$

$$[R2\text{-}TGF\beta_{\text{act}}]_s + [ALK5]_s \underset{k_{\text{sma2b}}}{\overset{k_{\text{sma2a}}}{\rightleftharpoons}} [ALK5\text{-}R2\text{-}TGF\beta_{\text{act}}]_s, \tag{8}$$

where ALK5 is a known TGFβRI and R2 is a generic TGFβRII. The resulting ALK5-R2-TGFβ_{act} receptor complex translocates to the cytoplasm, where it phosphorylates SMAD2 and SMAD3 signaling proteins. These phosphorylated SMADs then heterodimerize with SMAD4 to form the SMAD transcription factor complex.[44,45] Upon nuclear translocation, this complex promotes transcription of pro-fibrotic genes, driving fibroblastic differentiation of the VICs. Continued expression of these genes, including those involved in excessive extracellular matrix (ECM) production and overexpression of α smooth muscle actin (αSMA), leads to apoptosis. This process creates nucleation sites for calcium deposition, allowing hydroxyapatite, i.e., calcification, nodules to form.[46,47]

The SMAD signaling pathway model used in this work is adapted from Chung et al.[33] However, to fully capture the dynamics of SMAD signaling, we have modified the Chung et al. model to explicitly include SMAD3. Even though SMAD2 and SMAD3 exhibit similar cytoplasmic kinetics,[48] their roles diverge downstream: SMAD3 more strongly influences fibroblastic differentiation and ECM production,[49,50] making it the primary driver of the calcification response. Accordingly, following prior work by Arzani et al.,[21] we model calcification (Ca) as a first-order process driven by the SMAD transcription factor complex, with a rate constant that varies depending on whether the complex contains SMAD2 or SMAD3, i.e.,

$$[pSMAD2\text{-}SMAD4]_n \xrightarrow{k_{\text{sma27}}} [pSMAD2\text{-}SMAD4]_n + Ca \tag{9}$$

$$[pSMAD3\text{-}SMAD4]_n \xrightarrow{k_{\text{sma26}}} [pSMAD3\text{-}SMAD4]_n + Ca \tag{10}$$

Furthermore, the SMAD signaling pathway has an internal autoregulatory mechanism, i.e., the NO/cGMP/PKG pathway.[51,52] Activation of PKG by this pathway leads to hyperphosphorylation of SMAD3, inhibiting heterodimerization with SMAD4 and preventing translocatation to the nucleus.[28] Here, we model SMAD3 hyperphosphorylation as a bimolecular process,

$$[PKG_{\text{act}}] + [SMAD3]_c \xrightarrow{k_{\text{sma24}}} [PKG_{\text{act}}] + [pSMAD3_{\text{inh}}]_c \tag{11}$$

2.2.3 Endothelial NO regulation

Counteracting the pro-fibrotic SMAD pathway, the NO/cGMP/PKG signaling cascade, mediated by valvular endothelial cells (VECs), is initiated in response to high shear stress (Fig. 3). Upon valve opening, VECs lining the surface of the valve leaflets, particularly on the ventricularis (the side facing the left ventricle), experience elevated shear stress. This mechanical stimulus activates endothelial NO synthase (eNOS), leading to the production of NO,[6,52] which diffuses into the underlying VICs. There, it activates soluble guanylyl cyclase (sGC), catalyzing the conversion of guanosine triphosphate (GTP) to cGMP.[29] The NO regulation model used here is adapted from Garmaroudi et al.,[29] which includes sGC activation by NO and production of cGMP. In this work, we add two additional reactions that follow cGMP production: autoinhibitory PKG

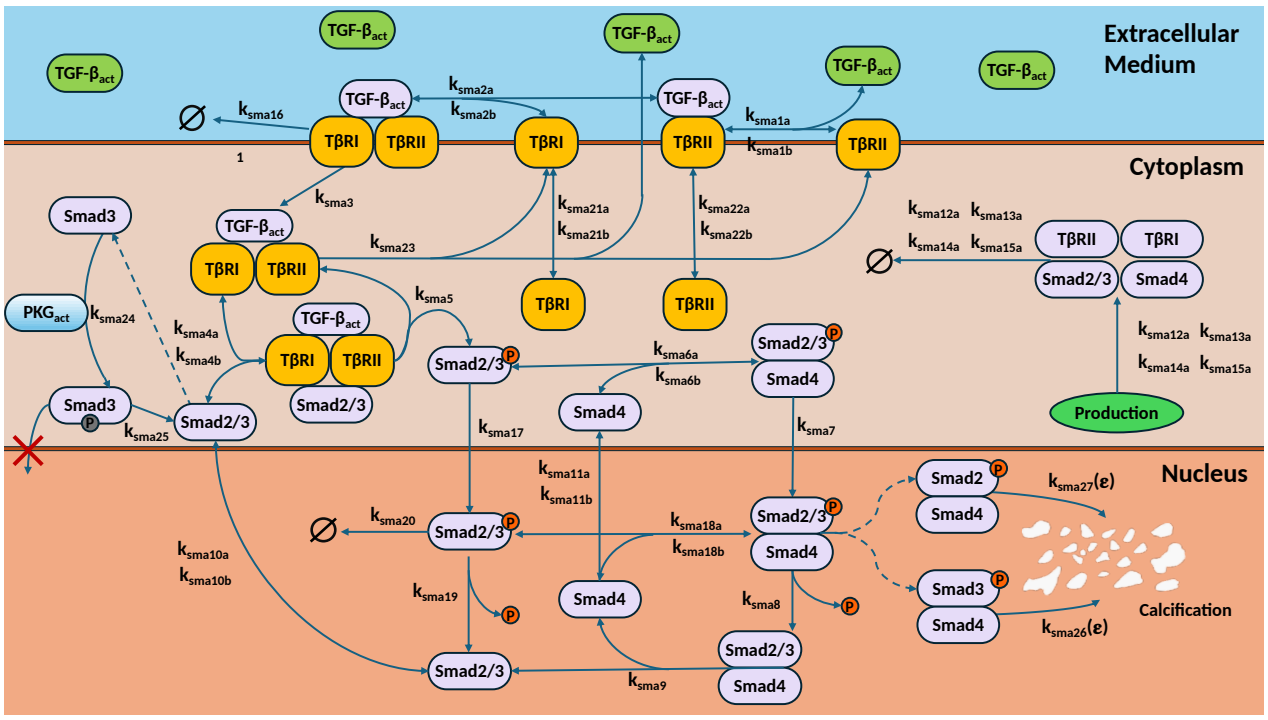

Figure 4: ***Mechanistic model of TGF-β–SMAD signaling leading to VIC calcification.*** *Active TGF-β binds sequentially to TGFβRII and TGFβRI at the VIC surface, forming a receptor complex that phosphorylates cytoplasmic SMAD2 and SMAD3. Phosphorylated SMADs heterodimerize with SMAD4 and translocate to the nucleus, where they promote pro-calcific gene expression. SMAD2 and SMAD3 are treated with identical kinetics except for PKG-dependent hyperphosphorylation of SMAD3, which prevents its association with SMAD4. Active PKG (PKG_{act}) is supplied by the NO pathway (Fig. 3), providing the biochemical link through which WSS-dependent NO production inhibits SMAD3-driven calcification. Arrows denote biochemical reactions, and dashed arrows represent molecular transport between compartments.*

deactivation,[53] modeled as the first-order reaction $[PKG_{act}] \xrightarrow{\text{k}_{\text{inh10}}} [PKG]$, and recycling of GMP back to GTP. Although a multifaceted process,[54,55] for simplicity, here we model GMP recycling as the first-order process $[GMP] \xrightarrow{\text{k}_{\text{inh11}}} [GTP]$.

As a secondary messenger, cGMP induces smooth muscle relaxation by activating cGMP-dependent protein kinases, such as PKG, modeled here as

$$[cGMP] + [PKG] \xrightarrow{k_{\text{inh9}}} [cGMP] + [PKG_{\text{act}}]. \tag{12}$$

Activated PKG then inhibits pro-calcific signaling pathways, including those driven by SMAD3[53] (see Eq. (11)). Although this pathway mitigates the progression of calcific nodule formation, its cardioprotective effects are limited. Persistent ECM production by quiescent VICs, along with leaflet damage that facilitates increased LDL and monocyte infiltration, compromises the effectiveness of NO signaling. These factors contribute to progressive valve leaflet thickening, which alters the shear stress environment and further impairs NO-mediated protection.[9]

2.2.4 Model parameters and simulation protocol

All biochemical reactions and corresponding ordinary differential equations (ODEs) for the three sub-models (Figs. 3 and 4) comprising the SB model of aortic calcification (Fig. 1) are provided in the Supporting Information in Tables. S1–S3 and Eqs. (S1)–(S46), respectively. Model parameters are provided in Tables S4–S6 and initial species concentrations in Table S7. In the case of the inflammation pathway model (Fig. 3, *left*), concentration and rate constant units had to be converted from cellular concentration to volume concentration to be consistent with the units in the SMAD signaling (Fig. 4) and NO regulation (Fig. 3, *right*) models. The valvular tissue properties used for this purpose are provided in Table 1.

Table 1: *Tissue properties used to convert units of rate constants and initial conditions in the SB model. Note that the foam cell formation ratio, α, is the ratio of the rates for LDL oxidation and foam cell formation. This factor is used to convert units in the inflammation pathway to be consistent with those for the other two modules.*

Parameter	Value	Definition	Reference
S	12 cm^2	Total surface area of leaflets	Current FSI model setup
S_{vic}	6 cm^2	Total area of VICs	Current FSI model setup
V_{vec}	2×10^{-12} L	Volume of a VEC	Khang et al.[56]
ρ_{vec}	10 000 cells/cm^2	VEC cell surface density	Ground et al.[57]
ρ_{vic}	50 000 cells/cm^2	VIC cell tissue density	Aikawa et al.,[58] Lis et al.[59]
α	5.7×10^{-6} cells/g	Foam cell formation ratio	Arzani et al.[21]

The three sub-models of the SB model were constructed and integrated in the open-source modeling and simulation platform PySB,[60] which is designed to facilitate and streamline the construction and analysis of complex biochemical models. Molecular and cellular processes are defined as reaction "rules",[61,62] which can be used to generate the coupled set of ODEs governing the system dynamics. These ODEs can then be solved numerically using ODE integrators implemented in SciPy,[63] which are callable from within PySB. This modular architecture is especially advantageous for our purposes, since each signaling pathway, based on different models from the literature, uses a different unit system. By encoding each sub-model as a separate PySB module, unit consistency can be achieved programmatically, allowing for easy simulation of the full integrated SB model.

3 Results

3.1 A multiscale framework for coupling FSI and SB models

We adopt a one-way coupling approach for the FSI-SB framework (Fig. 1). Our strategy is to first run an FSI simulation for one cardiac cycle, T, with assumed valve material properties to obtain averaged WSS and tissue strain. The WSS and strain information are then passed to the SB model as input to simulate the biochemical processes driving calcification. Both the WSS and tissue strain are calculated at each mesh node on a finite-element mesh of the valve. We use the spatial-temporal averaged WSS (SA-WSS), $\bar{\tau}$, which is averaged over each side, S, of the leaflets over the interval T,

$$\bar{\tau} = \frac{1}{ST}\int_0^T \int_{\partial\Omega} \tau(s,t)\, dA dt. \tag{13}$$

The initial value of the SA-WSS, $\bar{\tau}_0$, is obtained from the FSI simulation. Similarly, the temporally averaged maximum tissue strain is defined as

$$\bar{\epsilon} = \frac{1}{T}\int_0^T \max_{\Omega} |\epsilon(s,t)|\, dt, \tag{14}$$

where Ω is the tissue domain and the maximum value is taken over Ω at any time point. The initial value, $\bar{\epsilon}_0$, is also obtained from the FSI simulation. Both $\bar{\tau}_0$ and $\bar{\epsilon}_0$ are passed to the SB model.

In the SB model, the WSS and strain information, $\bar{\tau}$ and $\bar{\epsilon}$, are utilized as follows:

(1) The base rate constants for LDL and monocyte penetration in the absence of WSS are $\overline{k}_{\text{inf1}}$ and $\overline{k}_{\text{inf5}}$, respectively. The ODEs derived from the inflammation pathway are

$$[\dot{LDL}] = \underbrace{k_{\text{inf1}}}_{\text{subendothelial LDL penetration}} - \underbrace{k_{\text{inf2}}[LDL]}_{\text{LDL out diffusion}} - \underbrace{k_{\text{inf3}}[LDL]}_{\text{LDL oxidation}} \tag{15}$$

$$[\dot{Monocyte}] = \underbrace{k_{\text{inf5}}[oxLDL]}_{\text{baseline monocyte capture}} - \underbrace{k_{\text{inf6}}[Monocyte]}_{\text{monocyte-to-macrophage differentiation}} - \underbrace{k_{\text{inf7}}[Monocyte]}_{\text{monocyte apoptosis}} \tag{16}$$

In the presence of WSS, $\overline{k}_{\text{inf1}}$ and $\overline{k}_{\text{inf5}}$ are augmented by multiplying a stress-dependent factor to reflect decreases in response,[21] i.e.,

$$k_{\text{inf1}}(\bar{\tau}) = \frac{\overline{k}_{inf1}}{1 + \bar{\tau}/\bar{\tau}_{\text{ref}}} \tag{17}$$

$$k_{\text{inf5}}(\bar{\tau}) = \frac{\overline{k}_{inf5}}{1 + \bar{\tau}/\bar{\tau}_{\text{ref}}}, \tag{18}$$

where the reference WSS, $\bar{\tau}_{\text{ref}}$, is set to 2 Pa to represent the healthy valve case. These relationships are implemented because high WSS has been shown to reinforce endothelial junctions, leading to reduced transendothelial transport of macromolecules such as LDL, and decreased adhesion of immune cells, like monocytes. This inverse relationship between shear stress and vascular permeability has been demonstrated in animal models.[64,65]

(2) The production rate of NO is WSS-dependent, giving

$$[\dot{NO}] = \underbrace{k_{\text{NO}}(\bar{\tau})}_{\text{flow-induced NO production}} + \underbrace{k_{\text{inh1b}}[NO\text{-}sGC]}_{\text{NO unbinding from sGC}} - \underbrace{k_{\text{inh1a}}[NO]}_{\text{NO degradation}} - \underbrace{k_{\text{inh1a}}[NO][sGC]}_{\text{NO binding to sGC}}, \tag{19}$$

where $k_{\text{NO}}(\bar{\tau})$ is based on data from Sriram et al.[36] (see Fig. S1).

(3) Mechanical strains in the valvular tissue amplify calcification, in part by upregulating SMAD signaling. Increased strain promotes the aggregation of VICs, which limits their ability to migrate and redistribute across the tissue. This localized crowding not only intensifies paracrine TGF-β signaling, the activator of SMAD2/3, but also predisposes VICs to apoptosis or necroptosis within these dense clusters. The resulting apoptotic bodies and matrix vesicles serve as nucleation sites for calcific nodule formation.[8] Through this sequence, strain acts as both a mechanical and biochemical amplifier of calcification. Following a similar approach as Arzani et al.,[21] we account for the effects of strain by assuming it directly impacts the rate constants for calcium production by SMAD2/3, k_{sma26} and k_{sma27}, respectively (see Eqs. (9) and (10)), according to

$$k_{\text{sma26}} = \gamma k_c \left(1 + h_e\right) \tag{20}$$

$$k_{\text{sma27}} = \gamma \xi k_c \left(1 + h_e\right) \tag{21}$$

$$h_e = a_0(e^{a_1 \bar{\epsilon}} - 1). \tag{22}$$

Here, γ is a unit conversion factor from calcium nodules/well to Agatston score (data associated with these parameters from Ref. 8 are in units of nodules/well), k_c is the baseline calcification rate constant (in nodules/well/(M·s)), and $a_0 = 4.435 \times 10^4$ and $a_1 = 6.404$ are unitless strain magnification coefficients.[21] In the absence of strain ($\bar{\epsilon} = 0$), $h_e = 0$ and there is no strain magnification, giving $k_{\text{sma26}} = \gamma k_c$ and $k_{\text{sma27}} = \gamma \xi k_c$. Here, ξ is a scaling factor between 0 and 1 that represents the relative percentage of calcification by SMAD2 vs. SMAD3. Since SMAD3 is significantly more implicative of calcification,[49,50] we assume $\xi = 0.15$.

Since we only consider one-way coupling, and thus the effects of calcification on tissue stiffness and FSI are not simulated, we incorporate a simple feedback of calcification directly to WSS and tissue strain,

$$\bar{\tau} = \bar{\tau}_0 \, e^{-k_{\text{td}} \cdot \mathit{Calcification}} \tag{23}$$

$$\bar{\epsilon} = \frac{0.2 \, \mathit{Calcification} + 1}{\mathit{Calcification} + 1/\bar{\epsilon}_0}, \tag{24}$$

where *Calcification* is given in Agatston score.[66] The updated WSS and strain feed back to calcification through Eqs. (17)–(19) and (20)–(22). In this feedback model, the SA-WSS is assumed to decrease exponentially with increasing calcification. When *Calcification* $= 0$, the shear stress is simply its initial value obtained from the FSI simulation, i.e., $\bar{\tau} = \bar{\tau}_0$. As calcium nodules grow, the resulting changes in the valve's material properties significantly impair its ability to open, which generally reduces tissue strain. According to Eq. (24), $\bar{\epsilon} = \bar{\epsilon}_0$

in this case. As calcification progresses and becomes severe, $\bar{\epsilon} \to 0.2$, which is representative of the typical strain observed in calcified valves.[18,67] Although strain can exceed 0.2 in extreme cases, here we assume that calcification does not further affect strain beyond this threshold, an assumption consistent with prior modeling studies.[20,21] Note that these prior studies also included stress and strain updates. Here, we have generalized the approach to handle multiple cases as input variables. Additionally, k_{td} in Eq. (23) is used to adjust the feedback relations, and is set here to 0.006 Agatston^{-1}.

To summarize, the coupled FSI-SB framework proceeds by first running an FSI simulation of the aortic valve with specified properties (see *Methods and Models*). From the flow field and tissue deformation, WSS and strain information is obtained from Eqs. (13) and (14). The SB model is then simulated (see *Methods and Models*), described by the coupled set of ODEs

$$\dot{\mathbf{y}} = \mathbf{f}(\mathbf{y}; \bar{\tau}_0, \bar{\epsilon}_0), \qquad \mathbf{f} : \mathbb{R}^n \to \mathbb{R}^n, \qquad \mathbf{y}(\mathbf{0}) = \mathbf{y_0}, \tag{25}$$

where $\mathbf{y} \in \mathbb{R}^n$ is the solution vector of concentrations for all biochemical species involved in the calcification process. Initial conditions for the SB model are given in Table S7. All other species, including complexes, are assumed to have zero initial concentrations.

3.2 The coupled FSI–SB model predicts earlier high-risk calcification for low-average-shear, thickened aortic valves

To demonstrate the application of the coupled FSI–SB framework, we simulated long-term aortic valve calcification for three representative leaflet thicknesses: 0.3, 0.5, and 0.75 mm. For each case, SA-WSS and temporally averaged strain obtained from the FSI simulations were used to drive the biochemical dynamics governing inflammation, SMAD activation, and calcium deposition (Fig. 5). The model predicts a clear dependence of calcification rate on leaflet thickness. The thinnest leaflet (0.3 mm) shows the slowest increase in calcium accumulation, reaching an Agatston score of 400, the clinically defined high-risk threshold, at approximately 20.8 years. The 0.5-mm leaflet reaches the same threshold earlier, at roughly 18.8 years. These values fall within the range of moderate progression rates reported in clinical studies, where calcification increases steadily but remains well below the rapid progression observed in the most severely affected patients.[68] The thickest leaflet (0.75 mm), representing a pathological case, exhibits the fastest progression, exceeding the 0.3-mm trajectory by nearly five years and reaching high-risk calcification earliest. These results illustrate how relatively small changes in leaflet thickness can lead to large differences in long-term calcification trajectories.

3.3 FSI simulations reveal an inverse relationship between leaflet thickness and average WSS and strain

The FSI simulations reveal systematic differences in valve kinematics, flow rate, shear stress, and tissue deformation across the three leaflet thicknesses considered (0.3, 0.5, 0.75 mm). Flow visualizations show that the 0.3-mm leaflet generates a strong, coherent systolic jet with substantial downstream vortical structures, while the 0.5-mm leaflet produces a weaker jet, and the 0.75-mm leaflet exhibits markedly reduced flow coherence due to its restricted opening (Fig. 6a). These differences are reflected quantitatively in the geometric orifice area (GOA): the 0.3-mm leaflet reaches a maximum GOA of 2.05 cm^2, the 0.5-mm leaflet opens to 1.91 cm^2, and the 0.75-mm leaflet achieves only 0.80 cm^2 (Fig. 6b). Flow rate curves follow the same ordering, with peak systolic flow highest for the 0.3-mm leaflet and lowest for the 0.75-mm leaflet (Fig. 6c). These findings align with previously reported hemodynamic consequences of leaflet thickening and stiffening.[1,2]

Differences in WSS also track consistently with leaflet thickness. Figures 6d–e show that average WSS on both the aortic and ventricular sides decreases in magnitude as thickness increases. Although wall shear stress levels are substantially higher on the ventricular side (approximately an order of magnitude greater than on the aortic side), the same thickness-dependent trend is observed on both surfaces. Spatial WSS distributions on the ventricular side further illustrate these trends: although the 0.5-mm leaflet exhibits slightly higher local shear than the 0.3-mm leaflet, reflecting its reduced bending near the attachment edge and closer alignment with the incoming jet, this difference is minimal, and the two cases remain nearly indistinguishable after spatial

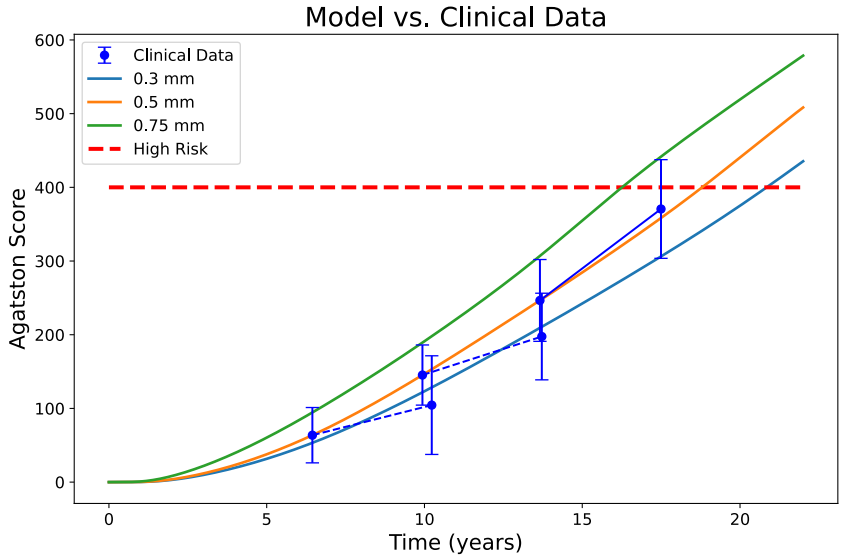

Figure 5: *Long-term calcification trajectories predicted by the coupled FSI–SB model compared with clinical data. Model predictions for leaflet thicknesses of 0.3, 0.5, and 0.75 mm are shown over 23 years. Thinner valves accumulate calcium more slowly, while thicker valves reach the high-risk Agatston threshold years earlier. Clinical measurements from a cohort of 70 patients[68] (solid blue line with markers) and two subgroups (lowest and mid terciles; dashed lines) are included for comparison. The slopes of the clinical data illustrate moderate progression rates that align with the 0.3-mm and 0.5-mm model trajectories.*

averaging. In contrast, the 0.75-mm leaflet shows a markedly different pattern, with high shear concentrated primarily along the free edge and much lower shear elsewhere, producing a substantially reduced average WSS due to its restricted opening and diminished flow acceleration. (Fig. 7a). Numerical values of peak and mean WSS for each case are summarized in Table 2.

Table 2: ***Key outputs from the FSI simulations.*** *h: leaflet thickness, E_B: bending rigidity, $\bar{\tau}_0$: SA-WSS, $\bar{\epsilon}_0$: maximum strain, V_{valve}: valve tissue volume, $GOA_{\max}$: maximum GOA, V_{stroke}: stroke volume.*

h (mm)	E_B (Pa·m)	$\bar{\tau}_0$ (Pa)	$\bar{\epsilon}_0$	V_{valve} (L)	$\text{GOA}_{\max}$ (cm^2)	V_{stroke} (mL)
0.3	5.36×10^{-6}	2.23	0.270	1.876×10^{-4}	2.05	88.18
0.5	2.48×10^{-5}	2.36	0.262	3.127×10^{-4}	1.91	74.81
0.75	8.37×10^{-5}	1.33	0.236	4.690×10^{-4}	0.80	19.81

Leaflet deformation follows the same monotonic ordering. The maximum principal strain curves in Fig. 6f and the spatial distributions in Fig. 7b show that the 0.3-mm leaflet undergoes the greatest deformation throughout systole, with high-strain regions covering substantial portions of the leaflet surface. The 0.5-mm leaflet displays intermediate deformation, whereas the 0.75-mm leaflet exhibits minimal strain. These trends are also reflected in the strain values reported in Table 2. Together, these results (Figs. 6, 7 and Table 2) demonstrate that increasing leaflet thickness consistently reduces leaflet opening, peak flow rate, WSS, and tissue strain. This establishes a clear inverse relationship between leaflet thickness and the mechanical environment that drives downstream biochemical signaling.

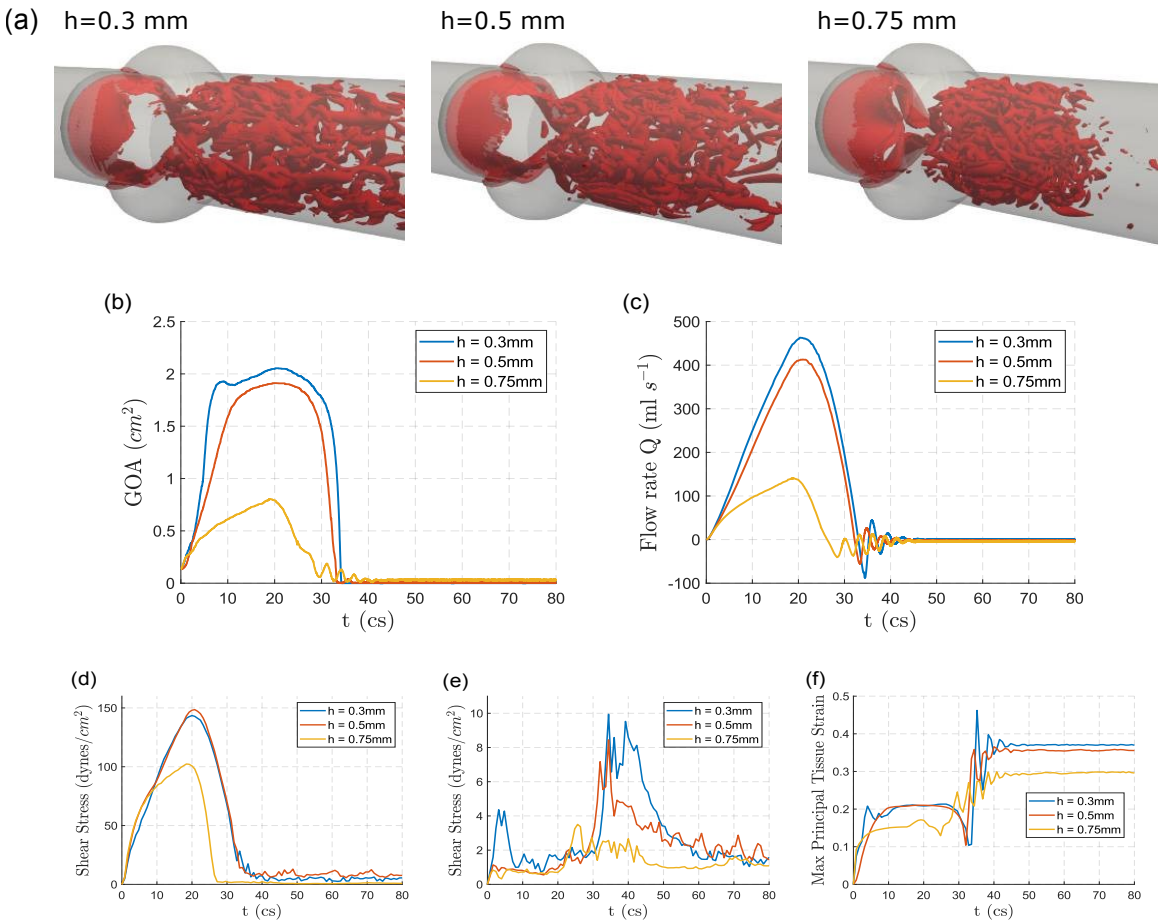

Figure 6: ***Leaflet thickening diminishes valve opening, weakens systolic flow, and reduces shear and strain.*** *(a) Instantaneous systolic flow fields (t = 20 cs) for leaflet thicknesses of 0.3, 0.5, and 0.75 mm, visualized using the Q2-criterion, showing progressive weakening and loss of coherence in the systolic jet. (b) Geometric orifice area (GOA), where thicker leaflets not only achieve smaller peak opening but also close earlier in systole, indicating reduced mobility. (c) Flow rate curves showing diminished peak systolic flow and earlier cessation of forward flow for thicker leaflets. (d,e) SA-WSS on the ventricular (d) and aortic (e) surfaces. Ventricular-side WSS exhibits smooth temporal profiles across all three thicknesses, reflecting the predominantly unidirectional shear environment on this surface. In contrast, aortic-side WSS displays pronounced fluctuations due to its intrinsically low-magnitude, multidirectional shear environment, yet still shows a general reduction in shear levels as thickness increases. (f) Maximum principal tissue strain, showing the greatest deformation for the 0.3-mm leaflet and minimal strain for the 0.75-mm leaflet.*

3.4 Reduced shear in thicker aortic valves decreases NO production, cGMP synthesis, and PKG activation

The long-term outputs of the NO inhibition module reflect the differences in mechanical loading established by the FSI simulations. Because endothelial NO production is strongly dependent on shear stress, the reduced WSS levels associated with thicker valves (Section 3.3) translate directly into lower concentrations of NO throughout the simulated 23-year period (Fig. 8a). The 0.3- and 0.5-mm cases exhibit similar NO trajectories during the early years of the simulation, while the 0.75-mm leaflet shows a noticeably attenuated response beginning at early time points and progressively diverging over time.

These reductions in NO propagate immediately to downstream components of the pathway. The cGMP concentrations produced by soluble guanylate cyclase decrease with leaflet thickness, with the thickest leaflet generating the lowest cGMP levels (Fig. 8b). Activated PKG (PKG_{act}) exhibits the same trend: the 0.3- and 0.5-mm valves maintain higher PKG_{act} levels for most of the simulated duration, whereas the 0.75-mm case shows reduced activation throughout (Fig. 8c). The similar shapes of the curves for NO, cGMP, and PKG_{act}

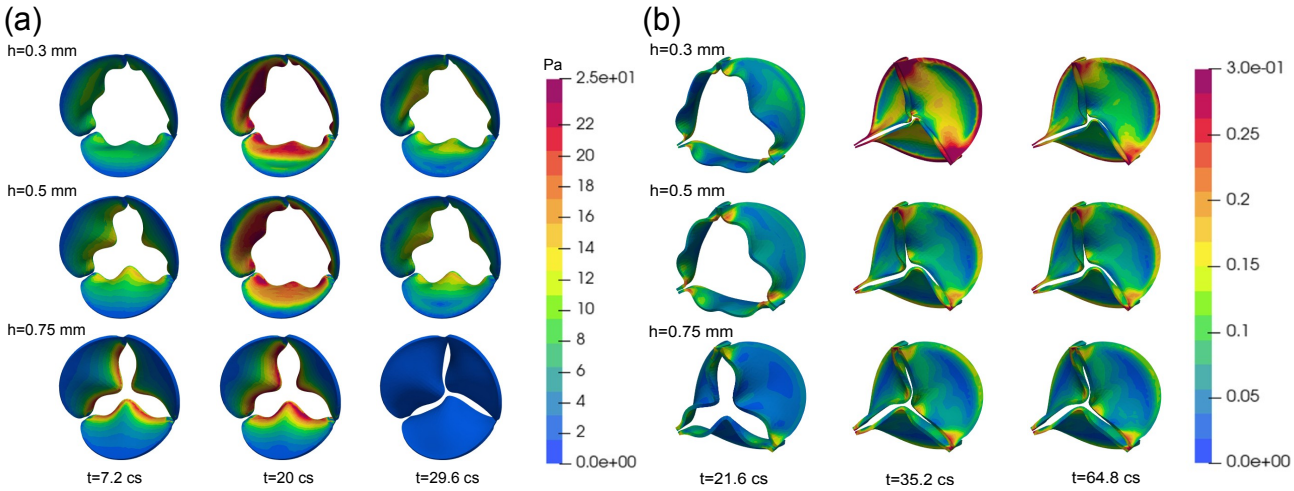

Figure 7: ***Contours of ventricular wall shear stress and aortic-side tissue strain across leaflet thicknesses.*** *(a) Ventricular-side contours of WSS shown on the deforming valve at key systolic time points for leaflet thicknesses of 0.3, 0.5, and 0.75 mm. Thinner leaflets generate larger openings and broad regions of elevated WSS across the ventricular surface at peak systole, whereas the restricted 0.75-mm leaflet produces much lower WSS overall, with the remaining high-shear regions concentrated primarily along the leaflet-free edge due to its limited opening and reduced flow acceleration. (b) Aortic-side contours of maximum principal strain at three time points sampled throughout the cardiac cycle. Strain levels are highest during diastole, when the leaflets close and experience significant bending near the commissures and free edges. Thinner leaflets display substantially higher diastolic strain, while the thickest leaflet exhibits markedly reduced deformation across all phases.*

reflect the fast and tightly coupled dynamics of the NO module, where shear-driven fluctuations propagate rapidly. Taken together, these results show that variations in leaflet thickness lead to sustained differences in NO bioavailability and downstream cGMP and PKG activation. The monotonic ordering of these responses across the three thicknesses follows the ordering of WSS magnitudes from the FSI model, establishing a direct mechanochemical link between reduced shear and diminished biochemical signaling within the NO pathway.

3.5 Lower WSS in thicker aortic valves increases LDL and monocyte penetration and elevates downstream TGF-β activation

The inflammation module reveals that reductions in WSS due to increased leaflet thickness (Fig. 6d,e) lead to distinct differences in lipid infiltration and inflammatory activation over long timescales. LDL concentrations rise more rapidly and reach higher levels in the 0.75-mm leaflet compared to the 0.3-mm and 0.5-mm cases, producing an early and persistent separation between the pathological and physiological thicknesses (Fig. 9a). Although LDL levels in all cases eventually converge toward similar values by the end of the 23-year simulation, the elevated LDL burden in the early years of the 0.75-mm case establishes downstream differences in the subsequent inflammatory cascade. These differences are partly reflected in the oxidized LDL (oxLDL) dynamics. While oxLDL peaks early in all simulations, the 0.75-mm leaflet exhibits a modestly higher initial peak before all cases converge to similar levels after approximately two years (Fig. 9b). Despite the transient nature of these oxLDL differences, they are sufficient to produce noticeable changes in monocyte recruitment. Monocyte concentrations show a small early spike that is highest for the thickest leaflet case (Fig. 9c), after which they return to comparable levels across all valve thicknesses.

In contrast to monocytes, the macrophage and foam cell populations show large and persistent differences among the three cases. Both populations increase throughout the simulated period, but the 0.75-mm leaflet maintains substantially higher macrophage (Fig. 9d) and foam cell (Fig. 9e) levels than the 0.3-mm and 0.5-mm cases across the entire 23-year timeframe. This sustained divergence arises despite the relatively small and short-lived differences in oxLDL and monocyte levels, highlighting the sensitivity of the inflammatory

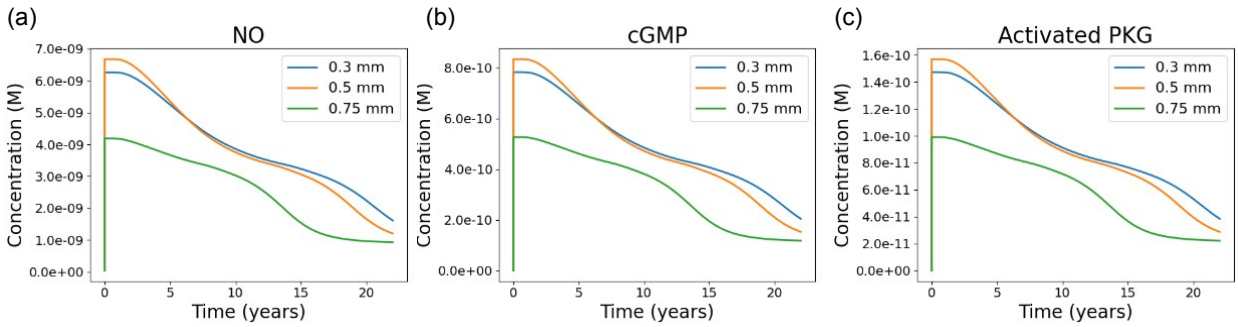

Figure 8: ***Long-term biochemical trajectories of the NO/cGMP/PKG pathway for valves of differing thickness.*** *(a) NO concentration over 23 years for leaflet thicknesses of 0.3, 0.5, and 0.75 mm, where the thicker leaflets experience overall lower WSS, resulting in reduced NO production. (b) cGMP concentration over time, where the reduced NO levels in the thicker valves lead to lower cGMP generation. (c) Activated PKG concentrations, which depend on cGMP. Lower cGMP in the thicker valves causes PKG to activate in lower quantities as well. All three trajectories exhibit similar temporal shapes due to the tightly coupled reaction kinetics within the NO signaling module.*

module to early perturbations in lipid infiltration. The effects of these inflammatory differences propagate to the TGF-β subsystem. Latent TGF-β rises more quickly in the 0.75-mm case and reaches a higher early peak before gradually declining and converging with the 0.5-mm case (Fig. 9f). Activated TGF-β, however, shows a persistent separation across all cases, with the 0.75-mm leaflet maintaining the highest levels throughout the simulation, followed by 0.5-mm and then 0.3-mm (Fig. 9g). Because macrophages and foam cells contribute to TGF-β activation, their sustained elevation in the thickest-leaflet case likely drives the long-term divergence observed in activated TGF-β. These results show that even modest, short-lived differences in LDL infiltration and oxLDL exposure can amplify through the nonlinear inflammatory cascade, producing long-lasting differences in macrophage and foam cell populations and, ultimately, sustained elevation of activated TGF-β in thicker, low-shear valves.

3.6 Thicker valves exhibit increased total SMAD phosphorylation and reduced SMAD3 inhibition, leading to enhanced pro-calcific signaling

The SMAD signaling module integrates the combined biochemical inputs from the upstream pathways driven by WSS, NO availability, and TGF-β activation. Because total phosporylated SMAD (pSMAD2/3) formation depends on active TGF-β (TGF-β_{act}) while phosphorylated SMAD3 (pSMAD3) inhibition depends on active PKG (PKG_{act}), the SMAD responses reflect the trends established in the mechanical (Figs. 6 and 7), NO inhibition (Fig. 8), and inflammation (Fig. 9) results. The model captures the expected SMAD signaling behavior in response to these thickness-dependent upstream cues (Fig. 10). Nuclear pSMAD2 concentrations rise monotonically across all cases, with the 0.75-mm leaflet producing the highest pSMAD2 levels due to its elevated TGF-β_{act} concentrations (Fig. 10a). Cytoplasmic pSMAD2 exhibits a similar ordering (Fig. 10c). Nuclear pSMAD3 also displays an amplified response in the thickest leaflet, but with a distinct transient peak followed by a decline (Fig. 10b). This peak arises from the combined influence of higher TGF-β_{act} levels (Fig. 9g) and lower PKG_{act} levels (Fig. 8c). The cytoplasmic pSMAD3 profiles follow the same pattern (Fig. 10d).

The inhibited pSMAD3 trajectories further illustrate the importance of PKG-mediated repression of SMAD3. The 0.3- and 0.5-mm cases show higher inhibited pSMAD3, reflecting their stronger NO/PKG responses (Fig. 8) and lower TGF-β_{act} concentrations (Fig. 9g). In contrast, the 0.75-mm leaflet exhibits markedly reduced SMAD3 inhibition (Fig. 10e), consistent with both diminished PKG_{act} and sustained TGF-β_{act} production. These results show that thicker aortic valve leaflets exhibit increased total SMAD2/3 phosphorylation and reduced PKG-dependent SMAD3 inhibition. The resulting elevation in transcriptionally active pSMAD3 provides a direct pro-calcific signal within the integrated signaling network, connecting the upstream mechanical and biochemical differences (Figs. 6–9) to the accelerated calcification trajectory observed for thicker valves (Fig. 5).

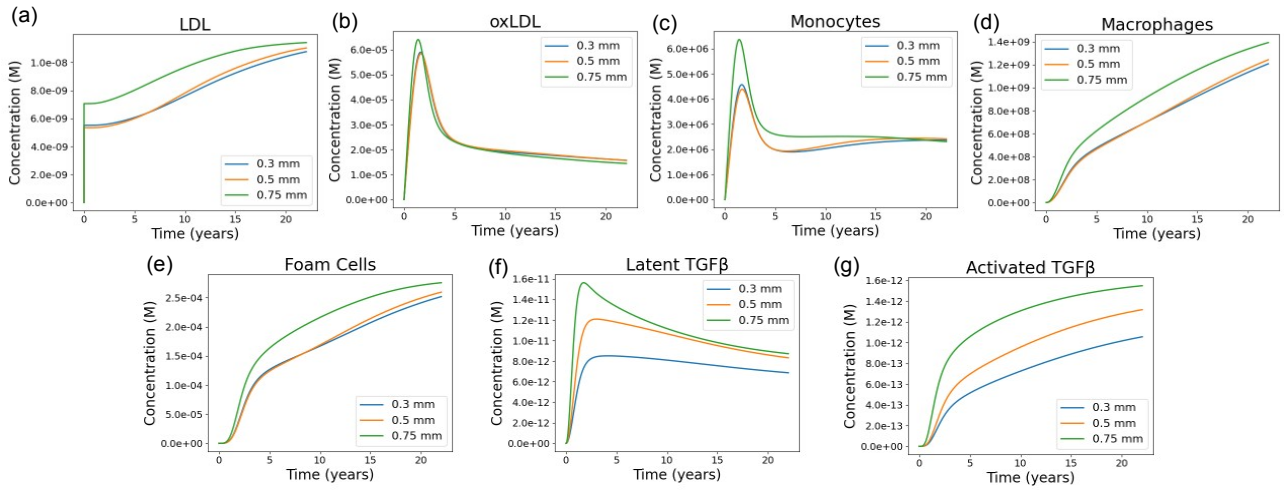

Figure 9: ***Long-term trajectories of inflammatory and TGF-β–related species for valves of differing thickness.*** *(a, b) LDL and oxLDL concentrations over 23 years for leaflet thicknesses of 0.3, 0.5, and 0.75 mm. Lower shear in the thicker valves leads to greater LDL accumulation, producing higher oxLDL levels. For oxLDL, the three curves exhibit a short-lived difference around the 2-year mark, after which they converge, though this early divergence still propagates downstream. (c–e) Monocytes, macrophages, and foam cells, which evolve sequentially through monocyte recruitment, macrophage differentiation, and macrophage uptake of oxLDL. Monocyte levels also show a brief early separation near the 2-year peak before aligning, while macrophages and foam cells display more persistent differences, with thicker valves consistently generating larger populations due to elevated upstream oxLDL and LDL levels. (f, g) Latent and activated TGF-β concentrations, produced downstream of foam cell activity. Latent TGF-β trajectories partially converge after their early peak, but activated TGF-β maintains clear separation across leaflet thicknesses, reflecting sustained differences in upstream inflammatory signaling.*

4 Discussion

We present a mechanochemical framework that couples 3D FSI with systems-level biochemical signaling to model CAVD progression. By supplying FSI-derived shear stresses and tissue strains directly to an integrated SB model of NO signaling, inflammatory activation, and TGF-β/SMAD activation (Fig. 1), the coupled FSI-SB framework captures how differences in leaflet thickness translate into distinct early biochemical events and, ultimately, divergent long-term calcification trajectories. Unlike prior approaches that treat hemodynamics and biochemical signaling in isolation, this architecture enables direct evaluation of how valve-scale mechanics affect intracellular and extracellular pathways that regulate calcification over years. This extensible multiphysics platform enables linking aortic valve hemodynamics to biochemical determinants of disease.

As a proof-of-principle demonstration of the platform, we quantified how leaflet thickness alters flow-induced mechanical forces and biochemical signaling in aortic valves, resulting in divergent long-term calcification. Coupled FSI-SB simulations show that thinner, more compliant valves maintain higher shear and stronger NO-mediated inhibition, while thicker, fibrotic valves exhibit reduced shear, enhanced TGF-β activation, and accelerated calcification (Fig. 5). FSI results reveal that thinner leaflets maintain larger orifice areas, stronger flow jets, higher WSS, and greater tissue strains, whereas thicker leaflets open less and experience systematically reduced mechanical loading (Figs. 6, 7, and Table 2). At the biochemical level, reduced WSS leads to lower NO levels and diminished cGMP and PKG activation over a $>$ 20-year simulated period (Fig. 8), consistent with prior reports that shear-dependent NO signaling suppresses early pro-calcific activity.[6] Lower WSS also increases LDL penetration (Fig. 9a), producing transient differences in oxLDL and monocyte recruitment (Fig. 9b,c). This causes persistent increases in macrophages and foam cells (Fig. 9d,e), in agreement with clinical and experimental observations that inflammatory loading accelerates CAVD progression.[5] These immune cell populations drive higher TGF-β activation in thicker leaflets (Fig. 9f,g), which is then amplified by the SMAD pathway. Cytoplasmic and nuclear pSMAD2 increase across all cases (Fig. 10a,c), while pSMAD3 exhibits an

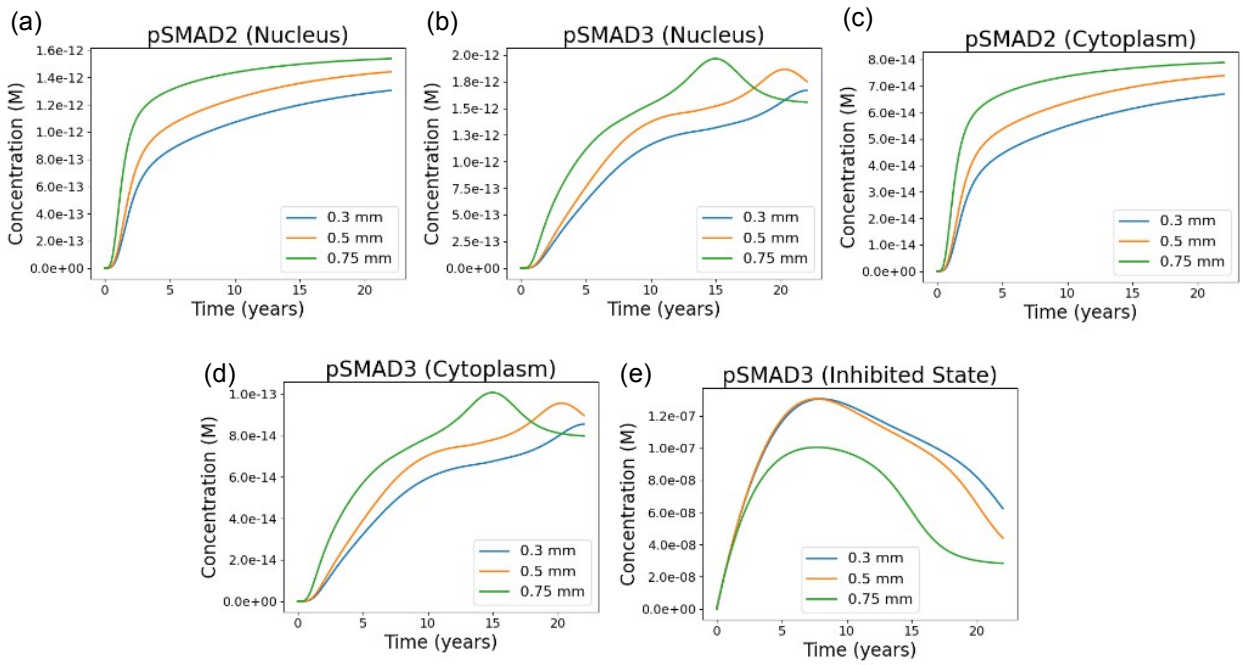

Figure 10: ***Long-term trajectories of SMAD2/3 signaling species for valves of differing thickness.*** *(a, b) Nuclear pSMAD2 and pSMAD3 concentrations over 23 years for leaflet thicknesses of 0.3, 0.5, and 0.75 mm. Nuclear pSMAD2 increases and then approaches a steady state, with thicker valves maintaining higher levels due to their elevated TGF-β activation. In contrast, nuclear pSMAD3 exhibits a transient peak followed by a decline, reflecting the competing influences of TGF-β–driven phosphorylation and PKG-mediated inhibition. The thickest valves sustain the highest overall pSMAD3 levels due to stronger TGF-β signaling and weaker PKG activity. (c, d) Cytoplasmic pSMAD2 and pSMAD3 show the same distinction: pSMAD2 rises toward a steady-state plateau, whereas pSMAD3 displays a peak-and-decline profile driven by the same balance between TGF-β and PKG. (e) Inhibited pSMAD3, produced through PKG-dependent hyperphosphorylation, is highest in the thinner valves, reflecting their stronger NO/cGMP/PKG signaling, and lowest in the thickest valve, consistent with diminished PKG activity and sustained TGF-β exposure.*

early peak due to competing influences of TGF-β and PKG (Fig. 10b,d). Reduced PKG-mediated inhibition in thicker valves results in a larger pool of active pSMAD3 (Fig. 10e), consistent with reports linking low shear and diminished NO signaling to accelerated calcification and poor clinical outcomes.[6] These interconnected mechanobiological effects collectively explain the observed divergent calcification trajectories (Fig. 5).

Despite these encouraging results, several limitations of the present FSI-SB framework should be noted. First, the current implementation uses a one-way coupling in which FSI-derived WSS and strain drive biochemical dynamics, but mechanical consequences of tissue calcification do not feed back to update leaflet deformation or flow. The phenomenological adjustments used to approximate stiffening effects (Eqs. 23 and 24) do not capture changes in leaflet geometry, nonuniform thickening, or coaptation. Fully two-way coupling between the FSI and SB modules will be essential for predictive modeling of advanced CAVD, and is an area of current effort (Fig. 1). Additional limitations include uncertainty in parameter values for the integrated SB model, many of which lack precise *in vivo* measurements. Although parameters were drawn from peer-reviewed sources, future versions would benefit from formal calibration or Bayesian parameter inference approaches.[69,70] The biochemical model also treats each leaflet as spatially well-mixed, while in reality calcification is heterogeneous. Incorporating spatial diffusion, regional variations in WSS and strain, and VIC heterogeneity will be needed to predict localized nodule formation. Finally, our use of a simplified leaflet geometry and straight aortic channel was intentional to isolate thickness-dependent effects, but limits direct clinical applicability. The underlying FSI solver supports patient-specific geometries,[71] enabling more clinically realistic extensions .

A major advantage of the present FSI-SB framework is its modular architecture, which provides significant

flexibility and opportunities for future development. The SB model can be readily expanded to include additional pathways implicated in CAVD, such as bone morphogenetic protein (BMP) signaling and SMAD1/5/7 regulation,[72] matrix metalloproteinase (MMP) activity,[73] NO-dependent S-nitrosylation,[74] and osteogenic differentiation of VICs.[75] The platform also supports simulation of pharmacological interventions by targeting specific biochemical reaction branches, enabling *in silico* exploration of mechanosensitive therapies. Incorporating spatial heterogeneity, patient-specific anatomy, and two-way coupling between leaflet mechanics and biochemical remodeling will further enhance the predictive and translational potential of the FSI-SB framework. The present work establishes a foundation for mechanobiological modeling of CAVD progression, with the long-term goal of supporting personalized diagnostics, risk stratification, and therapeutic design.

5 Conclusion

Computational modeling is becoming an essential tool for understanding and ultimately treating CAVD. As experimental techniques increasingly reveal the molecular and mechanical complexity of CAVD, there is a growing need for integrative frameworks capable of unifying these multiscale processes into coherent, predictive computational models. The framework developed in this study represents a step toward that goal by linking FSI with mechanistic biochemical signaling to simulate long-term disease progression. By capturing how changes in aortic leaflet mechanics reshape endothelial signaling, inflammatory activation, and SMAD-mediated transcription, the model illustrates the power of mechanochemical simulations to uncover pathways through which mechanical remodeling influences cellular decision-making. Although the present work focuses on leaflet thickening, the framework is sufficiently flexible to incorporate patient-specific geometries, emerging molecular pathways, and pharmacological perturbations. With future extensions, including two-way coupling, spatially resolved VIC dynamics, and calibrated biochemical parameter sets, the framework can support predictive analyses of disease progression and provide a platform for virtual testing of therapeutic interventions. As computational cardiology continues to advance, models of this type will play an increasingly central role in identifying early mechanobiological indicators of disease, evaluating potential treatment strategies, and personalizing care for patients with aortic valve pathology. The approach developed here demonstrates how high-fidelity FSI simulations and SB models can be integrated to generate mechanistic insight and inspire new strategies for preventing or slowing CAVD.

6 Supporting Information

The Supporting Information (SI) accompanying this manuscript provides a comprehensive description of the model formulation and implementation. It includes a complete listing of all biochemical reactions incorporated in the signaling network and the corresponding system of ordinary differential equations derived from them. Detailed parameter documentation is also provided, including rate constants, amplification factors, and other kinetic terms, along with their physiological justification and cited literature sources. Furthermore, the SI specifies the initial conditions used for each molecular species, their biological rationale, and references to experimental data from which these values were obtained. Together, these materials ensure full transparency and reproducibility of the computational model.

Acknowledgments

This work is funded by the National Science Foundation Graduate Research Fellowship Program (NSF-GRFP) to MQ (Award # 1937963 and 2444112) and a National Institutes of Health K22 Career Development Award (K22-CA37857) to LAH. The 3D FSI simulations were performed on the Stampede3 supercomputer at the Texas Advanced Computing Center (TACC) through the *Advanced Cyberinfrastructure Coordination Ecosystem: Services and Support (ACCESS)* program.

References

[1] Brian R Lindman, Marie-Annick Clavel, Patrick Mathieu, Bernard Iung, Patrizio Lancellotti, Catherine M Otto, and Philippe Pibarot. Calcific aortic stenosis. *Nature Reviews Disease Primers*, 2(1):1–28, 2016.

[2] Louis-Hippolyte Minvielle Moncla, Mewen Briend, Yohan Bossé, and Patrick Mathieu. Calcific aortic valve disease: mechanisms, prevention and treatment. *Nature Reviews Cardiology*, 20(8):546–559, 2023.

[3] Katherine E Yutzey, Linda L Demer, Simon C Body, Gordon S Huggins, Dwight A Towler, Cecilia M Giachelli, Marion A Hofmann-Bowman, Douglas P Mortlock, Melissa B Rogers, Mehran M Sadeghi, et al. Calcific aortic valve disease: a consensus summary from the Alliance of Investigators on Calcific Aortic Valve Disease. *Arteriosclerosis, Thrombosis, and Vascular Biology*, 34(11):2387–2393, 2014.

[4] Arkady Rutkovskiy, Anna Malashicheva, Gareth Sullivan, Maria Bogdanova, Anna Kostareva, Kåre-Olav Stensløkken, Arnt Fiane, and Jarle Vaage. Valve interstitial cells: the key to understanding the pathophysiology of heart valve calcification. *Journal of the American Heart Association*, 6(9):e006339, 2017.

[5] Petra Büttner, Lukas Feistner, Philipp Lurz, Holger Thiele, Joshua D Hutcheson, and Florian Schlotter. Dissecting calcific aortic valve disease—the role, etiology, and drivers of valvular fibrosis. *Frontiers in Cardiovascular Medicine*, 8:660797, 2021.

[6] Jennifer Richards, Ismail El-Hamamsy, Si Chen, Zubair Sarang, Padmini Sarathchandra, Magdi H Yacoub, Adrian H Chester, and Jonathan T Butcher. Side-specific endothelial-dependent regulation of aortic valve calcification: interplay of hemodynamics and nitric oxide signaling. *The American Journal of Pathology*, 182(5):1922–1931, 2013.

[7] Simon Kraler, Vidu Garg, and Alexander Akhmedov. Calcific aortic valve disease: novel insights into nitric oxide signalling. *European Heart Journal*, 43(17):1665–1667, 2022.

[8] Charles I Fisher, Joseph Chen, and W David Merryman. Calcific nodule morphogenesis by heart valve interstitial cells is strain dependent. *Biomechanics and Modeling in Mechanobiology*, 12:5–17, 2013.

[9] W David Merryman and Frederick J Schoen. Mechanisms of calcification in aortic valve disease: role of mechanokinetics and mechanodynamics. *Current Cardiology Reports*, 15:1–7, 2013.

[10] Charles S Peskin. Numerical analysis of blood flow in the heart. *Journal of Computational Physics*, 25(3):220–252, 1977.

[11] MD De Tullio, A Cristallo, E Balaras, and R Verzicco. Direct numerical simulation of the pulsatile flow through an aortic bileaflet mechanical heart valve. *Journal of Fluid Mechanics*, 622:259–290, 2009.

[12] Boyce E Griffith, Xiaoyu Luo, David M McQueen, and Charles S Peskin. Simulating the fluid dynamics of natural and prosthetic heart valves using the immersed boundary method. *International Journal of Applied Mechanics*, 1(01):137–177, 2009.

[13] Iman Borazjani. Fluid–structure interaction, immersed boundary-finite element method simulations of bio-prosthetic heart valves. *Computer Methods in Applied Mechanics and Engineering*, 257:103–116, 2013.

[14] Ming-Chen Hsu, David Kamensky, Yuri Bazilevs, Michael S Sacks, and Thomas JR Hughes. Fluid–structure interaction analysis of bioprosthetic heart valves: significance of arterial wall deformation. *Computational Mechanics*, 54(4):1055–1071, 2014.

[15] David Kamensky, Ming-Chen Hsu, Dominik Schillinger, John A Evans, Ankush Aggarwal, Yuri Bazilevs, Michael S Sacks, and Thomas JR Hughes. An immersogeometric variational framework for fluid–structure interaction: Application to bioprosthetic heart valves. *Computer Methods in Applied Mechanics and Engineering*, 284:1005–1053, 2015.

[16] Ye Chen and Haoxiang Luo. A computational study of the three-dimensional fluid–structure interaction of aortic valve. *Journal of Fluids and Structures*, 80:332–349, 2018.

[17] Ye Chen and Haoxiang Luo. Pressure distribution over the leaflets and effect of bending stiffness on fluid–structure interaction of the aortic valve. *Journal of Fluid Mechanics*, 883:A52, 2020.

[18] Ivan Vesely and Ronald Noseworthy. Micromechanics of the fibrosa and the ventricularis in aortic valve leaflets. *Journal of Biomechanics*, 25(1):101–113, 1992.

[19] Angelique Balguid, Mirjam P Rubbens, Anita Mol, Ruud A Bank, Ad JJC Bogers, Jorge P Van Kats, Bas AJM De Mol, Frank PT Baaijens, and Carlijn VC Bouten. The role of collagen cross-links in biomechanical behavior of human aortic heart valve leaflets—relevance for tissue engineering. *Tissue Engineering*, 13(7):1501–1511, 2007.

[20] Susumu Katayama, Nobuyuki Umetani, Toshiaki Hisada, and Seiryo Sugiura. Bicuspid aortic valves undergo excessive strain during opening: a simulation study. *The Journal of Thoracic and Cardiovascular Surgery*, 145(6):1570–1576, 2013.

[21] Amirhossein Arzani, Kristyn S Masters, and Mohammad RK Mofrad. Multiscale systems biology model of calcific aortic valve disease progression. *ACS Biomaterials Science & Engineering*, 3(11):2922–2933, 2017.

[22] Giulia Di Tomaso, Vanessa Díaz-Zuccarini, and Cesar Pichardo-Almarza. A multiscale model of atherosclerotic plaque formation at its early stage. *IEEE Transactions on Biomedical Engineering*, 58(12):3460–3463, 2011.

[23] Myriam Cilla, Estefania Pena, and Miguel A Martinez. Mathematical modelling of atheroma plaque formation and development in coronary arteries. *Journal of The Royal Society Interface*, 11(90):20130866, 2014.

[24] Javid Azimi-Boulali, Gretchen J Mahler, Bruce T Murray, and Peter Huang. Multiscale computational modeling of aortic valve calcification. *Biomechanics and Modeling in Mechanobiology*, 23(2):581–599, 2024.

[25] Fali Zhao, Yi Wu, Wei Yang, Dongdong Wu, Can Wang, and Fengmin Zhang. Inhibition of vascular calcification by microRNA-155-5p is accompanied by the inactivation of TGF-β1/Smad2/3 signaling pathway. *Acta Histochemica*, 122(4):151551, 2020.

[26] Hadi Khalil, Onur Kanisicak, Vikram Prasad, Robert N Correll, Xing Fu, Tobias Schips, Ronald J Vagnozzi, Ruijie Liu, Thanh Huynh, Se-Jin Lee, et al. Fibroblast-specific TGF-β–Smad2/3 signaling underlies cardiac fibrosis. *The Journal of Clinical Investigation*, 127(10):3770–3783, 2017.

[27] Mrinmay Chakrabarti, Aniket Bhattacharya, Mengistu G Gebere, John Johnson, Zeeshan A Ayub, Ioulia Chatzistamou, Narendra R Vyavahare, and Mohamad Azhar. Increased TGFβ1 and SMAD3 contribute to age-related aortic valve calcification. *Frontiers in Cardiovascular Medicine*, 9:770065, 2022.

[28] Peng Li, Dajun Wang, Jason Lucas, Suzanne Oparil, Dongqi Xing, Xu Cao, Lea Novak, Matthew B Renfrow, and Yiu-Fai Chen. Atrial natriuretic peptide inhibits transforming growth factor β–induced Smad signaling and myofibroblast transformation in mouse cardiac fibroblasts. *Circulation Research*, 102(2):185–192, 2008.

[29] Farshid S Garmaroudi, Diane E Handy, Yang-Yu Liu, and Joseph Loscalzo. Systems pharmacology and rational polypharmacy: nitric oxide-cyclic GMP signaling pathway as an illustrative example and derivation of the general case. *PLoS Computational Biology*, 12(3):e1004822, 2016.

[30] Fang-Bao Tian, Hu Dai, Haoxiang Luo, James F Doyle, and Bernard Rousseau. Fluid–structure interaction involving large deformations: 3D simulations and applications to biological systems. *Journal of Computational Physics*, 258:451–469, 2014.

[31] Seung Hyun Lee and Jae-Hoon Choi. Involvement of immune cell network in aortic valve stenosis: communication between valvular interstitial cells and immune cells. *Immune Network*, 16(1):26, 2016.

[32] Mohamed J Nsaibia, Anichavezhi Devendran, Eshak Goubaa, Jamal Bouitbir, Romain Capoulade, and Rihab Bouchareb. Implication of lipids in calcified aortic valve pathogenesis: why did statins fail? *Journal of Clinical Medicine*, 11(12):3331, 2022.

[33] Seung-Wook Chung, Fayth L Miles, Robert A Sikes, Carlton R Cooper, Mary C Farach-Carson, and Babatunde A Ogunnaike. Quantitative modeling and analysis of the transforming growth factor β signaling pathway. *Biophysical Journal*, 96(5):1733–1750, 2009.

[34] Pontus Melke, Henrik Jönsson, Evangelia Pardali, Peter ten Dijke, and Carsten Peterson. A rate equation approach to elucidate the kinetics and robustness of the TGF-β pathway. *Biophysical Journal*, 91(12):4368–4380, 2006.

[35] Bernhard Schmierer, Alexander L Tournier, Paul A Bates, and Caroline S Hill. Mathematical modeling identifies Smad nucleocytoplasmic shuttling as a dynamic signal-interpreting system. *Proceedings of the National Academy of Sciences*, 105(18):6608–6613, 2008.

[36] Krishna Sriram, Justin G Laughlin, Padmini Rangamani, and Daniel M Tartakovsky. Shear-induced nitric oxide production by endothelial cells. *Biophysical Journal*, 111(1):208–221, 2016.

[37] Yosuke Kanno, Takeshi Into, Charles J Lowenstein, and Kenji Matsushita. Nitric oxide regulates vascular calcification by interfering with TGF-β signalling. *Cardiovascular Research*, 77(1):221–230, 2008.

[38] Alexia Hulin, Alexandre Hego, Patrizio Lancellotti, and Cécile Oury. Advances in pathophysiology of calcific aortic valve disease propose novel molecular therapeutic targets. *Frontiers in Cardiovascular Medicine*, 5:21, 2018.

[39] Haoxiang Luo, Hu Dai, Paulo JSA Ferreira de Sousa, and Bo Yin. On the numerical oscillation of the direct-forcing immersed-boundary method for moving boundaries. *Computers & Fluids*, 56:61–76, 2012.

[40] Javier Bonet and Richard D. Wood. *Nonlinear Continuum Mechanics for Finite Element Analysis*. Cambridge University Press, 2nd edition, 2008.

[41] Ming-Chen Hsu, David Kamensky, Fei Xu, Josef Kiendl, Chenglong Wang, Michael CH Wu, Joshua Mineroff, Alessandro Reali, Yuri Bazilevs, and Michael S Sacks. Dynamic and fluid–structure interaction simulations of bioprosthetic heart valves using parametric design with T-splines and Fung-type material models. *Computational Mechanics*, 55:1211–1225, 2015.

[42] Fatemeh Salemizadehparizi, Peter Huang, Mei-Hsiu Chen, and Gretchen J Mahler. The contributions of increased reactive oxygen species and inflammatory macrophages to the development of aortic valve calcification. *Free Radical Biology and Medicine*, 2025.

[43] Ziqin Deng, Tao Fan, Chu Xiao, He Tian, Yujia Zheng, Chunxiang Li, and Jie He. TGF-β signaling in health, disease and therapeutics. *Signal Transduction and Targeted Therapy*, 9(1):61, 2024.

[44] Jia-Wei Wu, Robert Fairman, Jack Penry, and Yigong Shi. Formation of a stable heterodimer between Smad2 and Smad4. *Journal of Biological Chemistry*, 276(23):20688–20694, 2001.

[45] Masahiro Kawabata, Hirofumi Inoue, Aki Hanyu, Takeshi Imamura, and Kohei Miyazono. Smad proteins exist as monomers in vivo and undergo homo- and hetero-oligomerization upon activation by serine/threonine kinase receptors. *The EMBO Journal*, 1998.

[46] Huan Wang, Leslie A Leinwand, and Kristi S Anseth. Roles of transforming growth factor-β1 and OB-cadherin in porcine cardiac valve myofibroblast differentiation. *The FASEB Journal*, 28(10):4551, 2014.

[47] Meghan A Bowler, Matthew R Bersi, Larisa M Ryzhova, Rachel J Jerrell, Aron Parekh, and W David Merryman. Cadherin-11 as a regulator of valve myofibroblast mechanobiology. *American Journal of Physiology-Heart and Circulatory Physiology*, 315(6):H1614–H1626, 2018.

[48] Gareth J Inman, Francisco J Nicolás, and Caroline S Hill. Nucleocytoplasmic shuttling of Smads 2, 3, and 4 permits sensing of TGF-β receptor activity. *Molecular Cell*, 10(2):283–294, 2002.

[49] Laurie MG de Kroon, Roberto Narcisi, Guus GH Van Den Akker, Elly L Vitters, Esmeralda N Blaney Davidson, Gerjo JVM van Osch, and Peter M van der Kraan. SMAD3 and SMAD4 have a more dominant role than SMAD2 in TGFβ-induced chondrogenic differentiation of bone marrow-derived mesenchymal stem cells. *Scientific Reports*, 7(1):43164, 2017.

[50] Kathleen Flanders, Misako Sato, Akira Ooshima, Angelo Russo, and Anita Roberts. Smad-3 as a mediator of the fibrotic response. *International Journal of Experimental Pathology*, 85(1):A13–A13, 2004.

[51] Katherine Driscoll, Alexander D Cruz, and Jonathan T Butcher. Inflammatory and biomechanical drivers of endothelial-interstitial interactions in calcific aortic valve disease. *Circulation Research*, 128(9):1344–1370, 2021.

[52] Joan Fernández Esmerats, Jack Heath, and Hanjoong Jo. Shear-sensitive genes in aortic valve endothelium. *Antioxidants & Redox Signaling*, 25(7):401–414, 2016.

[53] Rajesh Sharma, Jeong Joo Kim, Liying Qin, Philipp Henning, Madoka Akimoto, Bryan VanSchouwen, Gundeep Kaur, Banumathi Sankaran, Kevin R MacKenzie, Giuseppe Melacini, et al. An auto-inhibited state of protein kinase G and implications for selective activation. *eLife*, 11:e79530, 2022.

[54] Nikolina Sekulic, Ludmila Shuvalova, Oliver Spangenberg, Manfred Konrad, and Arnon Lavie. Structural characterization of the closed conformation of mouse guanylate kinase. *Journal of Biological Chemistry*, 277(33):30236–30243, 2002.

[55] Ioan Lascu and Philippe Gonin. The catalytic mechanism of nucleoside diphosphate kinases. *Journal of Bioenergetics and Biomembranes*, 32(3):237–246, 2000.

[56] Alex Khang, Quan Nguyen, Xinzeng Feng, Daniel P Howsmon, and Michael S Sacks. Three-dimensional analysis of hydrogel-imbedded aortic valve interstitial cell shape and its relation to contractile behavior. *Acta Biomaterialia*, 163:194–209, 2023.

[57] Marcus Ground, Young Eun Park, Steve Waqanivavalagi, Karen Callon, Robert Walker, Paget Milsom, and Jillian Cornish. Generating robust human valvular interstitial cell cultures: Protocol and considerations. *Journal of Molecular and Cellular Cardiology*, 173:118–126, 2022.

[58] Elena Aikawa, Peter Whittaker, Mark Farber, Karen Mendelson, Robert F Padera, Masanori Aikawa, and Frederick J Schoen. Human semilunar cardiac valve remodeling by activated cells from fetus to adult: implications for postnatal adaptation, pathology, and tissue engineering. *Circulation*, 113(10):1344–1352, 2006.

[59] Grzegorz J Lis, Andrzej Dubrowski, Maciej Lis, Bernard Solewski, Karolina Witkowska, Veronika Aleksandrovych, Ewa Jasek-Gajda, Mateusz K Hołda, Krzysztof Gil, and Jan A Litwin. Identification of CD34+/PGDFRα+ valve interstitial cells (VICs) in human aortic valves: association of their abundance, morphology and spatial organization with early calcific remodeling. *International Journal of Molecular Sciences*, 21(17):6330, 2020.

[60] Carlos F Lopez, Jeremy L Muhlich, John A Bachman, and Peter K Sorger. Programming biological models in Python using PySB. *Molecular Systems Biology*, 9(1):646, 2013.

[61] Lily A Chylek, Leonard A Harris, Chang-Shung Tung, James R Faeder, Carlos F Lopez, and William S Hlavacek. Rule-based modeling: a computational approach for studying biomolecular site dynamics in cell signaling systems. *Wiley interdisciplinary reviews. Systems biology and medicine*, 6:13–36, 8 2014.

[62] Lily A Chylek, Leonard A Harris, James R Faeder, and William S Hlavacek. Modeling for (physical) biologists: an introduction to the rule-based approach. *Physical Biology*, 12:045007, 7 2015.

[63] Pauli Virtanen, Ralf Gommers, Travis E Oliphant, Matt Haberland, Tyler Reddy, David Cournapeau, Evgeni Burovski, Pearu Peterson, Warren Weckesser, Jonathan Bright, Stéfan J van der Walt, Matthew Brett, Joshua Wilson, K Jarrod Millman, Nikolay Mayorov, Andrew R J Nelson, Eric Jones, Robert Kern, Eric Larson, C J Carey, İlhan Polat, Yu Feng, Eric W Moore, Jake VanderPlas, Denis Laxalde, Josef Perktold, Robert Cimrman, Ian Henriksen, E A Quintero, Charles R Harris, Anne M Archibald, Antônio H Ribeiro, Fabian Pedregosa, Paul van Mulbregt, Aditya Vijaykumar, Alessandro Pietro Bardelli, Alex Rothberg, Andreas Hilboll, Andreas Kloeckner, Anthony Scopatz, Antony Lee, Ariel Rokem, C Nathan Woods, Chad Fulton, Charles Masson, Christian Häggström, Clark Fitzgerald, David A Nicholson, David R Hagen, Dmitrii V Pasechnik, Emanuele Olivetti, Eric Martin, Eric Wieser, Fabrice Silva, Felix Lenders, Florian Wilhelm, G Young, Gavin A Price, Gert-Ludwig Ingold, Gregory E Allen, Gregory R Lee, Hervé Audren, Irvin Probst, Jörg P Dietrich, Jacob Silterra, James T Webber, Janko Slavič, Joel Nothman, Johannes Buchner, Johannes Kulick, Johannes L Schönberger, José Vinícius de Miranda Cardoso, Joscha Reimer, Joseph Harrington, Juan Luis Cano Rodríguez, Juan Nunez-Iglesias, Justin Kuczynski, Kevin Tritz, Martin Thoma, Matthew Newville, Matthias Kümmerer, Maximilian Bolingbroke, Michael Tartre, Mikhail Pak, Nathaniel J Smith, Nikolai Nowaczyk, Nikolay Shebanov, Oleksandr Pavlyk, Per A Brodtkorb, Perry Lee, Robert T McGibbon, Roman Feldbauer, Sam Lewis, Sam Tygier, Scott Sievert, Sebastiano Vigna, Stefan Peterson, Surhud More, Tadeusz Pudlik, Takuya Oshima, Thomas J Pingel, Thomas P Robitaille, Thomas Spura, Thouis R Jones, Tim Cera, Tim Leslie, Tiziano Zito, Tom Krauss, Utkarsh Upadhyay, Yaroslav O Halchenko, Yoshiki Vázquez-Baeza, and SciPy 1.0 Contributors. SciPy 1.0: fundamental algorithms for scientific computing in Python. *Nature Methods*, 17:261–272, 2020.

[64] Heather A Himburg, Deborah M Grzybowski, Andrew L Hazel, Jeffrey A LaMack, Xue-Mei Li, and Morton H Friedman. Spatial comparison between wall shear stress measures and porcine arterial endothelial permeability. *American Journal of Physiology-Heart and Circulatory Physiology*, 286(5):H1916–H1922, 2004.

[65] Swetha Rathan, Casey J Ankeny, Sivakkumar Arjunon, Zannatul Ferdous, Sandeep Kumar, Joan Fernandez Esmerats, Jack M Heath, Robert M Nerem, Ajit P Yoganathan, and Hanjoong Jo. Identification of side-and shear-dependent microRNAs regulating porcine aortic valve pathogenesis. *Scientific Reports*, 6(1):25397, 2016.

[66] Lea Azour, Michael A Kadoch, Thomas J Ward, Corey D Eber, and Adam H Jacobi. Estimation of cardiovascular risk on routine chest CT: Ordinal coronary artery calcium scoring as an accurate predictor of Agatston score ranges. *Journal of Cardiovascular Computed Tomography*, 11(1):8–15, 2017.

[67] K Jane Grande, Richard P Cochran, Per G Reinhall, and Karyn S Kunzelman. Stress variations in the human aortic root and valve: the role of anatomic asymmetry. *Annals of Biomedical Engineering*, 26:534–545, 1998.

[68] David Messika-Zeitoun, Lawrence F Bielak, Patricia A Peyser, Patrick F Sheedy, Stephen T Turner, Vuyisile T Nkomo, Jerome F Breen, Joseph Maalouf, Christopher Scott, A Jamil Tajik, et al. Aortic valve calcification: determinants and progression in the population. *Arteriosclerosis, Thrombosis, and Vascular Biology*, 27(3):642–648, 2007.

[69] Erin M Shockley, Jasper A Vrugt, and Carlos F Lopez. PyDREAM: high-dimensional parameter inference for biological models in Python. *Bioinformatics*, 34(4):695–697, 2018.

[70] Geena V Ildefonso, Marie Oliver Metzig, Alexander Hoffmann, Leonard A Harris, and Carlos F Lopez. A biochemical necroptosis model explains cell-type-specific responses to cell death cues. *Biophysical Journal*, 122(5):817–834, 2023.

[71] Y. Wang, Y. Cai, M. Pang, Y. Xu, G. Kassab, C. Zhou, G. Chase, X. Chen, H. Luo, and Y. Chen. Fluid–structure interaction of left ventricle with impaired ventricular contractility. *Acta Mechanica Sinica*, 2025. In press.

[72] M Victoria Gomez-Stallons, Elaine E Wirrig-Schwendeman, Keira R Hassel, Simon J Conway, and Katherine E Yutzey. Bone morphogenetic protein signaling is required for aortic valve calcification. *Arteriosclerosis, Thrombosis, and Vascular Biology*, 36(7):1398–1405, 2016.

[73] Emile R Mohler. Mechanisms of aortic valve calcification. *American Journal of Cardiology*, 94(11):1396–1402, 2004.

[74] Brian Lima, Michael T Forrester, Douglas T Hess, and Jonathan S Stamler. S-nitrosylation in cardiovascular signaling. *Circulation Research*, 106(4):633–646, 2010.

[75] Jane A Leopold. Cellular mechanisms of aortic valve calcification. *Circulation: Cardiovascular Interventions*, 5(4):605–614, 2012.

[76] Pei Jiang, Peng-ke YAN, Jian-xiong CHEN, Bing-yang ZHU, Xiao-yong LEI, Wei-dong YIN, and Duan-fang LIAO. High density lipoprotein 3 inhibits oxidized low density lipoprotein-induced apoptosis via promoting cholesterol efflux in RAW264.7 cells. *Acta Pharmacologica Sinica*, 27(2):151–157, 2006.

[77] Geetika Bajpai, Caralin Schneider, Nicole Wong, Andrea Bredemeyer, Maarten Hulsmans, Matthias Nahrendorf, Slava Epelman, Daniel Kreisel, Yongjian Liu, Akinobu Itoh, et al. The human heart contains distinct macrophage subsets with divergent origins and functions. *Nature Medicine*, 24(8):1234–1245, 2018.

[78] Iraida Sharina and Emil Martin. Cellular factors that shape the activity or function of nitric oxide-stimulated soluble guanylyl cyclase. *Cells*, 12(3):471, 2023.

[79] Nazish Sayed, Padmamalini Baskaran, Xiaolei Ma, Focco Van Den Akker, and Annie Beuve. Desensitization of soluble guanylyl cyclase, the NO receptor, by S-nitrosylation. *Proceedings of the National Academy of Sciences*, 104(30):12312–12317, 2007.

[80] Douglas D Thomas, Xiaoping Liu, Stephen P Kantrow, and Jack R Lancaster Jr. The biological lifetime of nitric oxide: implications for the perivascular dynamics of NO and O2. *Proceedings of the National Academy of Sciences*, 98(1):355–360, 2001.

[81] Sirada Srihirun, Barbora Piknova, Nathawut Sibmooh, and Alan N Schechter. Phosphorylated vasodilator-stimulated phosphoprotein (P-VASPSer239) in platelets is increased by nitrite and partially deoxygenated erythrocytes. *PLoS One*, 13(3):e0193747, 2018.

[82] Nazimuddin Khan, Parag P Shah, David Ban, Pablo Trigo-Mourino, Marta G Carneiro, Lynn DeLeeuw, William L Dean, John O Trent, Levi J Beverly, Manfred Konrad, et al. Solution structure and functional investigation of human guanylate kinase reveals allosteric networking and a crucial role for the enzyme in cancer. *Journal of Biological Chemistry*, 294(31):11920–11933, 2019.

[83] Edward E McKee, Alice T Bentley, Ronald M Smith Jr, Jonathan R Kraas, and Christina E Ciaccio. Guanine nucleotide transport by atractyloside-sensitive and-insensitive carriers in isolated heart mitochondria. *American Journal of Physiology-Cell Physiology*, 279(6):C1870–C1879, 2000.

[84] Eva Syková and Charles Nicholson. Diffusion in brain extracellular space. *Physiological Reviews*, 88(4):1277–1340, 2008.

[85] JB Bassingthwaighte, CY Wang, and IS3454538 Chan. Blood-tissue exchange via transport and transformation by capillary endothelial cells. *Circulation Research*, 65(4):997–1020, 1989.

[86] Guo-Wei He and Zhi-Gang Liu. Comparison of nitric oxide release and endothelium-derived hyperpolarizing factor–mediated hyperpolarization between human radial and internal mammary arteries. *Circulation*, 104(suppl_1):I–344, 2001.

[87] Alexandra Keilbach, Peter Ruth, and Franz Hofmann. Detection of cGMP dependent protein kinase isozymes by specific antibodies. *European Journal of Biochemistry*, 208(2):467–473, 1992.

7 Supplementary material

Reactions for the three sub-models of the SB model of aortic calcification

Table S1: *Inflammation model*

Reaction	Description
$\emptyset \xrightarrow{k_{inf1}} [LDL]$	LDL penetrates the endothelium and enters the leaflets
$[LDL] \xrightarrow{k_{inf2}} \emptyset$	LDL exits the leaflets through the endothelium
$[LDL] \xrightarrow{k_{inf3}} [oxLDL]$	LDL oxidation
$[oxLDL] + [Macrophage] \xrightarrow{k_{inf4}} [Foam\ Cell]$	Macrophages absorb oxLDL to become lipid-laden foam cells
$[oxLDL] \xrightarrow{k_{inf5}} [oxLDL] + [Monocyte]$	Oxidized LDL promotes monocyte capture by increasing endothelial adhesion molecule expression, enabling circulating monocytes to enter the valve leaflets
$[Monocyte] \xrightarrow{k_{inf6}} [Macrophage]$	Monocytes differentiate into macrophages
$[Monocyte] \xrightarrow{k_{inf7}} \emptyset$	Monocyte apoptosis
$[Macrophage] + [TGF\beta] \xrightarrow{k_{inf8}} [Macrophage] + [TGF\beta_{\text{act}}]$	Macrophages activate latent TGF-β
$[Foam\ Cell] + [TGF\beta] \xrightarrow{k_{inf8}} [Foam\ Cell] + [TGF\beta_{\text{act}}]$	Foam cells activate latent TGF-β
$[Foam\ Cell] \xrightarrow{k_{inf9}} \emptyset$	Foam cell apoptosis
$\emptyset \xrightarrow{k_{inf10}} [TGF\beta]$	TGF-β secretion by macrophages and foam cells; the rate saturates at high cell numbers
$[TGF\beta_{\text{act}}] \xrightarrow{k_{inf11}} \emptyset$	Activated TGF-β degrades
$[TGF\beta] \xrightarrow{k_{inf12}} \emptyset$	Latent TGF-β degrades
$[Macrophage] \xrightarrow{k_{inf13}} \emptyset$	Macrophage apoptosis

Table S2: *SMAD signaling model*

Reaction	Description
$[TGF\beta_{\text{act}}] + [R2]_s \underset{k_{sma1b}}{\overset{k_{sma1a}}{\rightleftharpoons}} [R2\text{-}TGF\beta_{\text{act}}]_s$	Activated TGF-β binds and unbinds from TGFβRII at the VIC surface
$[R2\text{-}TGF\beta_{\text{act}}]_s + [ALK5]_s \underset{k_{sma2b}}{\overset{k_{sma2a}}{\rightleftharpoons}} [ALK5\text{-}R2\text{-}TGF\beta_{\text{act}}]_s$	The TGFβ–TGFβRII complex binds and unbinds from ALK5 (TGFβRI)
$[ALK5\text{-}R2\text{-}TGF\beta_{\text{act}}]_s \overset{k_{sma3}}{\rightleftharpoons} [ALK5\text{-}R2\text{-}TGF\beta_{\text{act}}]_c$	The receptor complex moves between the cell surface and cytoplasm
$[ALK5\text{-}R2\text{-}TGF\beta_{\text{act}}]_c + [SMAD2]_c \underset{k_{sma4b}}{\overset{k_{sma4a}}{\rightleftharpoons}} [SMAD2\text{-}ALK5\text{-}R2\text{-}TGF\beta_{\text{act}}]_c$	The receptor complex binds and unbinds from SMAD2
$[ALK5\text{-}R2\text{-}TGF\beta_{\text{act}}]_c + [SMAD3]_c \underset{k_{sma4b}}{\overset{k_{sma4a}}{\rightleftharpoons}} [SMAD3\text{-}ALK5\text{-}R2\text{-}TGF\beta_{\text{act}}]_c$	The receptor complex binds and unbinds from SMAD3
$[SMAD2\text{-}ALK5\text{-}R2\text{-}TGF\beta_{\text{act}}]_c \xrightarrow{k_{sma5}} [ALK5\text{-}R2\text{-}TGF\beta_{\text{act}}]_c + [pSMAD2]_c$	Bound SMAD2 is phosphorylated by the receptor complex
$[SMAD3\text{-}ALK5\text{-}R2\text{-}TGF\beta_{\text{act}}]_c \xrightarrow{k_{sma5}} [ALK5\text{-}R2\text{-}TGF\beta_{\text{act}}]_c + [pSMAD3]_c$	Bound SMAD3 is phosphorylated by the receptor complex

Table S2 (*cont.*)

Reaction	Description
$[pSMAD2]_c + [SMAD4]_c \underset{k_{sma6b}}{\overset{k_{sma6a}}{\rightleftharpoons}} [pSMAD2\text{-}SMAD4]_c$	pSMAD2 heterodimerizes with SMAD4
$[pSMAD3]_c + [SMAD4]_c \underset{k_{sma6b}}{\overset{k_{sma6a}}{\rightleftharpoons}} [pSMAD3\text{-}SMAD4]_c$	pSMAD3 heterodimerizes with SMAD4
$[pSMAD2\text{-}SMAD4]_c \xrightarrow{k_{sma7}} [pSMAD2\text{-}SMAD4]_n$	pSMAD2–SMAD4 heterodimer translocates to the nucleus
$[pSMAD3\text{-}SMAD4]_c \xrightarrow{k_{sma7}} [pSMAD3\text{-}SMAD4]_n$	pSMAD3–SMMAD4 heterodimer translocates to the nucleus
$[pSMAD2\text{-}SMAD4]_n \xrightarrow{k_{sma8}} [SMAD2\text{-}SMAD4]_n$	Nuclear pSMAD2–SMAD4 is dephosphorylated
$[pSMAD3\text{-}SMAD4]_n \xrightarrow{k_{sma8}} [SMAD3\text{-}SMAD4]_n$	Nuclear pSMAD3–SMAD4 is dephosphorylated
$[SMAD2\text{-}SMAD4]_n \xrightarrow{k_{sma9}} [SMAD2]_n + [SMAD4]_n$	Nuclear SMAD2–SMAD4 heterodimer dissociates
$[SMAD3\text{-}SMAD4]_n \xrightarrow{k_{sma9}} [SMAD3]_n + [SMAD4]_n$	Nuclear SMAD3–SMAD4 heterodimer dissociates
$[SMAD2]_c \underset{k_{sma10b}}{\overset{k_{sma10a}}{\rightleftharpoons}} [SMAD2]_n$	SMAD2 shuttles between cytoplasm and nucleus
$[SMAD3]_c \underset{k_{sma10b}}{\overset{k_{sma10a}}{\rightleftharpoons}} [SMAD3]_n$	SMAD3 shuttles between cytoplasm and nucleus
$[SMAD4]_c \underset{k_{sma11b}}{\overset{k_{sma11a}}{\rightleftharpoons}} [SMAD4]_n$	SMAD4 shuttles between cytoplasm and nucleus
$\emptyset \underset{k_{sma12b}}{\overset{k_{sma12a}}{\rightleftharpoons}} [R2]_s$	TGFβRII is generated and degraded
$\emptyset \underset{k_{sma13b}}{\overset{k_{sma13a}}{\rightleftharpoons}} [ALK5]_s$	ALK5 (TGFβRI) is generated and degraded
$\emptyset \underset{k_{sma14b}}{\overset{k_{sma14a}}{\rightleftharpoons}} [SMAD2]_c$	SMAD2 is generated and degraded
$\emptyset \underset{k_{sma14b}}{\overset{k_{sma14a}}{\rightleftharpoons}} [SMAD3]_c$	SMAD3 is generated and degraded
$\emptyset \underset{k_{sma15b}}{\overset{k_{sma15a}}{\rightleftharpoons}} [SMAD4]_c$	SMAD4 is generated and degraded
$[ALK5\text{-}R2\text{-}TGF\beta_{\mathrm{act}}]_s \xrightarrow{k_{sma16}} \emptyset$	The surface receptor complex is degraded
$[pSMAD2]_c \xrightarrow{k_{sma17}} [pSMAD2]_n$	pSMAD2 translocates to the nucleus
$[pSMAD3]_c \xrightarrow{k_{sma17}} [pSMAD3]_n$	pSMAD3 translocates to the nucleus
$[pSMAD2]_n + [SMAD4]_n \underset{k_{sma18b}}{\overset{k_{sma18a}}{\rightleftharpoons}} [pSMAD2\text{-}SMAD4]_n$	Nuclear pSMAD2 binds and unbinds from SMAD4
$[pSMAD3]_n + [SMAD4]_n \underset{k_{sma18b}}{\overset{k_{sma18a}}{\rightleftharpoons}} [pSMAD3\text{-}SMAD4]_n$	Nuclear pSMAD3 binds and unbinds from SMAD4
$[pSMAD2]_n \xrightarrow{k_{sma19}} [SMAD2]_n$	Nuclear pSMAD2 is dephosphorylated
$[pSMAD3]_n \xrightarrow{k_{sma19}} [SMAD3]_n$	Nuclear pSMAD3 is dephosphorylated
$[pSMAD2]_n \xrightarrow{k_{sma20}} \emptyset$	Nuclear pSMAD2 is degraded
$[pSMAD3]_n \xrightarrow{k_{sma20}} \emptyset$	Nuclear pSMAD3 is degraded
$[R2]_s \underset{k_{sma21b}}{\overset{k_{sma21a}}{\rightleftharpoons}} [R2]_c$	TGFβRII moves between cytoplasm and surface
$[ALK5]_s \underset{k_{sma22b}}{\overset{k_{sma22a}}{\rightleftharpoons}} [ALK5]_c$	ALK5 moves between cytoplasm and surface
$[ALK5\text{-}R2\text{-}TGF\beta_{\mathrm{act}}]_c \xrightarrow{k_{sma23}} [ALK5\text{-}R2\text{-}TGF\beta_{\mathrm{act}}]_s$	The receptor complex returns from the cytoplasm to the surface

Table S2 (*cont.*)

Reaction	Description
$[PKG_{\text{act}}] + [SMAD3]_c \xrightarrow{k_{sma24}} [PKG_{\text{act}}] + [pSMAD3_{\text{inh}}]_c$	Active PKG inhibits SMAD3 by phosphorylating inhibitory sites that prevent SMAD4 binding
$[pSMAD3_{\text{inh}}]_c \xrightarrow{k_{sma25}} [SMAD3]_c$	Inhibited SMAD3 is restored to its active form
$[pSMAD3\text{-}SMAD4]_n \xrightarrow{k_{sma26}} [pSMAD3\text{-}SMAD4]_n + Ca$	Nuclear pSMAD3–SMAD4 heterodimer promotes calcium production via transcription of pro-calcific genes
$[pSMAD2\text{-}SMAD4]_n \xrightarrow{k_{sma27}} [pSMAD2\text{-}SMAD4]_n + Ca$	Nuclear pSMAD2–SMAD4 heterodimer promotes calcium production via transcription of pro-calcific genes

Table S3: *NO regulation model*

Reaction	Description
$\emptyset \xrightarrow{k_{NO}} [NO]$	NO production, with a shear-dependent rate constant
$[NO] + [sGC] \underset{k_{inh1b}}{\overset{k_{inh1a}}{\rightleftharpoons}} [NO\text{-}sGC]$	NO binds and unbinds from sGC
$[sGC] + [GTP] \underset{k_{inh2b}}{\overset{k_{inh2a}}{\rightleftharpoons}} [sGC\text{-}GTP]$	sGC binds and unbinds from GTP
$[NO\text{-}sGC] + [GTP] \underset{k_{inh3b}}{\overset{k_{inh3a}}{\rightleftharpoons}} [NO\text{-}sGC\text{-}GTP]$	NO–sGC complex binds and unbinds from GTP
$[sGC\text{-}GTP] \xrightarrow{k_{inh4}} [sGC] + [cGMP]$	sGC catalyzes conversion of GTP to cGMP
$[NO\text{-}sGC\text{-}GTP] \xrightarrow{k_{inh5}} [NO\text{-}sGC] + [cGMP]$	NO–sGC catalyzes conversion of GTP to cGMP
$[cGMP] + [PDE] \underset{k_{inh6b}}{\overset{k_{inh6a}}{\rightleftharpoons}} [PDE\text{-}cGMP]$	cGMP binds and unbinds from PDE
$[PDE\text{-}cGMP] \xrightarrow{k_{inh7}} [PDE] + [GMP]$	PDE hydrolyzes cGMP to GMP
$[NO] \xrightarrow{k_{inh8}} \emptyset$	NO degrades
$[cGMP] + [PKG] \xrightarrow{k_{inh9}} [cGMP] + [PKG_{\text{act}}]$	cGMP activates PKG
$[PKG_{\text{act}}] \xrightarrow{k_{inh10}} [PKG]$	Active PKG deactivates
$[GMP] \xrightarrow{k_{inh11}} [GTP]$	GMP recycles back to GTP

ODEs derived from the reactions in Tables S1–S3

$$[\dot{LDL}] = \underbrace{k_{inf1}(\bar{\tau})}_{\text{Subendothelial LDL penetration}} - \underbrace{k_{\text{inf2}}[LDL]}_{\text{LDL diffusing out}} - \underbrace{k_{\text{inf3}}[LDL]}_{\text{LDL oxidation}} \tag{S1}$$

$$[\dot{oxLDL}] = \underbrace{k_{\text{inf3}}[LDL]}_{\text{LDL oxidation}} - \underbrace{k_{\text{inf4}}[oxLDL][Macrophage]}_{\text{Foam cell formation}} \tag{S2}$$

$$[\dot{Monocyte}] = \underbrace{k_{\text{inf5}}(\bar{\tau})[oxLDL]}_{\text{Baseline monocyte capture}} - \underbrace{k_{\text{inf6}}[Monocyte]}_{\text{Monocyte differentiation to macrophage}} - \underbrace{k_{\text{inf7}}[Monocyte]}_{\text{Monocyte apoptosis}} \tag{S3}$$

$$[\dot{Macrophage}] = \underbrace{k_{\text{inf6}}[Monocyte]}_{\text{Monocyte differentiation to macrophage}} - \underbrace{k_{\text{inf4}}[oxLDL][Macrophage]}_{\text{Foam cell formation}} - \underbrace{k_{\text{inf13}}[Macrophage]}_{\text{Macrophage apoptosis}} \tag{S4}$$

$$[\dot{Foam\ Cell}] = \underbrace{k_{\text{inf4}}[oxLDL][Macrophage]}_{\text{Foam cell formation}} - \underbrace{k_{\text{inf9}}[Foam\ Cell]}_{\text{Foam cell apoptosis}} \tag{S5}$$

$$[\dot{TGF\beta}] = \underbrace{k_{\text{inf10}}}_{\text{LatentTGF-}\beta\text{ production}} - \underbrace{k_{\text{inf12}}[TGF\beta]}_{\text{LatentTGF-}\beta\text{ degradation}} - \underbrace{k_{\text{inf8}}([Foam\ Cell] + [Macrophage])[TGF\beta]}_{\text{TGF-}\beta\text{ activation}} \tag{S6}$$

$$[\dot{TGF\beta}_{\text{act}}] = \underbrace{k_{\text{inf8}}([Foam\ \ Cell] + [Macrophage])[TGF\beta]}_{\text{TGF-}\beta\text{ activation}} + \underbrace{k_{\text{sma1b}}[R2\text{-}TGF\beta_{\text{act}}]_s}_{\text{TGF-}\beta\text{ unbinds from R2 receptor}}$$
$$+ \underbrace{k_{\text{sma23}}[ALK5\text{-}R2\text{-}TGF\beta_{\text{act}}]_c}_{\text{Receptor complex breaks completely}} - \underbrace{k_{\text{sma1a}}[R2]_s[TGF\beta_{\text{act}}]}_{\text{TGF-}\beta\text{ binds to R2 receptor}} - \underbrace{k_{\text{inf11}}[TGF\beta_{\text{act}}]}_{\text{ActiveTGF-}\beta\text{ degradation}} \tag{S7}$$

$$[ALK5\text{-}R2\dot{\text{-}}TGF\beta_{\text{act}}]_s = \underbrace{k_{\text{sma2a}}[ALK5]_s[R2\text{-}TGF\beta_{\text{act}}]_s}_{\text{Receptor complex formation with ALK5}} - \underbrace{k_{\text{sma2b}}[ALK5\text{-}R2\text{-}TGF\beta_{\text{act}}]_s}_{\text{ALK5 dissociates from receptor complex}}$$
$$- \underbrace{k_{\text{sma3}}[ALK5\text{-}R2\text{-}TGF\beta_{\text{act}}]_s}_{\text{Receptor complex detaches from cell surface into cytoplasm}} - \underbrace{(k_{\text{sma16ld}} + k_{\text{sma16cd}})[ALK5\text{-}R2\text{-}TGF\beta_{\text{act}}]_s}_{\text{Ligand induced and constitutive degradation of receptor complex}} \tag{S8}$$

$$[\dot{ALK5}]_s = \underbrace{k_{\text{sma22b}}[ALK5]_c}_{\text{ALK5 receptor reattaches to surface}} + \underbrace{k_{\text{sma13a}}}_{\text{ALK5 receptor synthesis}} + \underbrace{k_{\text{sma2b}}[ALK5\text{-}R2\text{-}TGF\beta_{\text{act}}]_s}_{\text{ALK5 dissociates from receptor complex}}$$
$$- \underbrace{k_{\text{sma13b}}[ALK5]_s}_{\text{ALK5 receptor degredation}} - \underbrace{k_{\text{sma2a}}[ALK5]_s[R2\text{-}TGF\beta_{\text{act}}]_s}_{\text{Receptor complex formation with ALK5}} - \underbrace{k_{\text{sma22a}}[ALK5]_s}_{\text{ALK5 receptor goes into cytoplasm}} \tag{S9}$$

$$[\dot{ALK5}]_c = \underbrace{k_{\text{sma22a}}[ALK5]_s}_{\text{ALK5 receptor goes into cytoplasm}} - \underbrace{k_{\text{sma22b}}[ALK5]_c}_{\text{ALK5 receptor reattaches to surface}} \tag{S10}$$

$$[\dot{R2}]_s = \underbrace{k_{\text{sma12a}}}_{\text{R2 receptor synthesis}} + \underbrace{k_{\text{sma23}}[ALK5\text{-}R2\text{-}TGF\beta_{\text{act}}]_c}_{\text{Receptor complex breaks completely}} + \underbrace{k_{\text{sma21b}}[R2]_c}_{\text{R2 receptor reattaches to surface}}$$
$$+ \underbrace{k_{\text{sma1b}}[R2\text{-}TGF\beta_{\text{act}}]_s}_{\text{TGF-}\beta\text{ unbinds from R2 receptor}} - \underbrace{k_{\text{sma12b}}[R2]_s}_{\text{R2 receptor degradation}} - \underbrace{k_{\text{sma1a}}[R2]_s[TGF\beta_{\text{act}}]}_{\text{TGF-}\beta\text{ binds to R2 receptor}}$$
$$- \underbrace{k_{\text{sma21a}}[R2]_s}_{\text{R2 receptor goes into cytoplasm}} \tag{S11}$$

$$[\dot{R2}]_c = \underbrace{k_{\text{sma21a}}[R2]_s}_{\text{R2 receptor goes into cytoplasm}} - \underbrace{k_{\text{sma21b}}[R2]_c}_{\text{R2 receptor reattaches to surface}} \tag{S12}$$

$$[R2\text{-}\dot{TGF\beta}_{\text{act}}]_s = \underbrace{k_{\text{sma2b}}[ALK5\text{-}R2\text{-}TGF\beta_{\text{act}}]_s}_{\text{ALK5 dissociates from receptor complex}} + \underbrace{k_{\text{sma1a}}[R2]_s[TGF\beta_{\text{act}}]}_{\text{TGF-}\beta\text{ binds to R2 receptor}}$$
$$- \underbrace{k_{\text{sma2a}}[ALK5]_s[R2\text{-}TGF\beta_{\text{act}}]_s}_{\text{Receptor complex formation with ALK5}} - \underbrace{k_{\text{sma1b}}[R2\text{-}TGF\beta_{\text{act}}]_s}_{\text{TGF-}\beta\text{ unbinds from R2 receptor}} \tag{S13}$$

$$[ALK5\text{-}R2\dot{\text{-}}TGF\beta_{\text{act}}]_c = \underbrace{k_{\text{sma5}}([SMAD2\text{-}ALK5\text{-}R2\text{-}TGF\beta_{\text{act}}]_c + [SMAD3\text{-}ALK5\text{-}R2\text{-}TGF\beta_{\text{act}}]_c)}_{\text{Phosphorylation of SMAD2/3}}$$
$$+ \underbrace{k_{\text{sma3}}[ALK5\text{-}R2\text{-}TGF\beta_{\text{act}}]_s}_{\text{Receptor complex detaches from cell surface into cytoplasm}}$$
$$+ \underbrace{k_{\text{sma4b}}([SMAD2\text{-}ALK5\text{-}R2\text{-}TGF\beta_{\text{act}}]_c + [SMAD3\text{-}ALK5\text{-}R2\text{-}TGF\beta_{\text{act}}]_c)}_{\text{Receptor complex dissociates from SMAD2/3}}$$
$$- \underbrace{k_{\text{sma4a}}[ALK5\text{-}R2\text{-}TGF\beta_{\text{act}}]_c([SMAD2]_c + [SMAD3]_c)}_{\text{Receptor complex binds to SMAD2/3}} - \underbrace{k_{\text{sma23}}[ALK5\text{-}R2\text{-}TGF\beta_{\text{act}}]_c}_{\text{Receptor complex breaks completely}} \tag{S14}$$

$$[SM\dot{A}D2]_c = \underbrace{k_{\text{sma14a}}}_{\text{SMAD2/3 synthesis}} + \underbrace{k_{\text{sma4b}}[SMAD2\text{-}ALK5\text{-}R2\text{-}TGF\beta_{\text{act}}]_c}_{\text{Receptor complex dissociates from SMAD2/3}} + \underbrace{k_{\text{sma10b}}[SMAD2]_n}_{\text{Translocation out of nucleus}}$$
$$- \underbrace{k_{\text{sma14b}}[SMAD2]_c}_{\text{SMAD2/3 degredation}} - \underbrace{k_{\text{sma4a}}[SMAD2]_c[ALK5\text{-}R2\text{-}TGF\beta_{\text{act}}]_c}_{\text{Receptor complex binds to SMAD2/3}} - \underbrace{k_{\text{sma10a}}[SMAD2]_c}_{\text{Translocation into nucleus}} \quad \text{(S15)}$$

$$[SM\dot{A}D3]_c = \underbrace{k_{\text{sma14a}}}_{\text{SMAD2/3 synthesis}} + \underbrace{k_{\text{sma4b}}[SMAD3\text{-}ALK5\text{-}R2\text{-}TGF\beta_{\text{act}}]_c}_{\text{Receptor complex dissociates from SMAD2/3}} + \underbrace{k_{\text{sma10b}}[SMAD3]_n}_{\text{Translocation out of nucleus}}$$
$$+ \underbrace{k_{\text{sma25}}[pSMAD3_{\text{inh}}]_c}_{\text{Cytosolic pSMAD3 desphosphorylates}} - \underbrace{k_{\text{sma14b}}[SMAD3]_c}_{\text{SMAD2/3 degredation}} - \underbrace{k_{\text{sma4a}}[SMAD3]_c[ALK5\text{-}R2\text{-}TGF\beta_{\text{act}}]_c}_{\text{Receptor complex binds to SMAD2/3}}$$
$$- \underbrace{k_{\text{sma24}}[PKG_{\text{act}}][SMAD3]_c}_{\text{PKG inhibits SMAD3 via hyperphosphorylation}} - \underbrace{k_{\text{sma10a}}[SMAD3]_c}_{\text{Translocation into nucleus}} \quad \text{(S16)}$$

$$[SM\dot{A}D4]_c = \underbrace{k_{\text{sma15a}}}_{\text{SMAD4 synthesis}} + \underbrace{k_{\text{sma6b}}([pSMAD2\text{-}SMAD4]_c + [pSMAD3\text{-}SMAD4]_c)}_{\text{pSMAD2/3 unbinds from SMAD4}}$$
$$+ \underbrace{k_{\text{sma11b}}[SMAD4]_n}_{\text{SMAD4 translocates out of nucleus}} - \underbrace{k_{\text{sma15b}}[SMAD4]_c}_{\text{SMAD4 degredation}} - \underbrace{k_{\text{sma6a}}[SMAD4]_c([pSMAD2]_c + [pSMAD3]_c)}_{\text{pSMAD2/3 binds to SMAD4 to form pSMAD2/3-4 complex}}$$
$$- \underbrace{k_{\text{sma11a}}[SMAD4]_c}_{\text{SMAD4 translocates into nucleus}} \quad \text{(S17)}$$

$$[pSM\dot{A}D2]_c = \underbrace{k_{\text{sma5}}[SMAD2\text{-}ALK5\text{-}R2\text{-}TGF\beta_{\text{act}}]_c}_{\text{Receptor complex phosphorylates SMAD2/3}} + \underbrace{k_{\text{sma6b}}[pSMAD2\text{-}SMAD4]_c}_{\text{pSMAD2/3 unbinds from SMAD4}}$$
$$- \underbrace{k_{\text{sma6a}}[SMAD4]_c[pSMAD2]_c}_{\text{pSMAD2/3 binds to SMAD4 to form pSMAD2/3-4 complex}} - \underbrace{k_{\text{sma17}}[pSMAD2]_c}_{\text{pSMAD2/3 translocates into nucleus}} \quad \text{(S18)}$$

$$[pSM\dot{A}D3]_c = \underbrace{k_{\text{sma5}}[SMAD3\text{-}ALK5\text{-}R2\text{-}TGF\beta_{\text{act}}]_c}_{\text{Receptor complex phosphorylates SMAD2/3}} + \underbrace{k_{\text{sma6b}}[pSMAD3\text{-}SMAD4]_c}_{\text{pSMAD2/3 unbinds from SMAD4}}$$
$$- \underbrace{k_{\text{sma6a}}[SMAD4]_c[pSMAD3]_c}_{\text{pSMAD2/3 binds to SMAD4 to form pSMAD2/3-4 complex}} - \underbrace{k_{\text{sma17}}[pSMAD3]_c}_{\text{pSMAD2/3 translocates into nucleus}} \quad \text{(S19)}$$

$$[SMAD2\text{-}ALK5\dot{\text{-}}R2\text{-}TGF\beta_{\text{act}}]_c = \underbrace{k_{\text{sma4a}}[SMAD2]_c[ALK5\text{-}R2\text{-}TGF\beta_{\text{act}}]_c}_{\text{Receptor complex binds to SMAD2/3}}$$
$$- \underbrace{(k_{\text{sma4b}} + k_{\text{sma5}})[SMAD2\text{-}ALK5\text{-}R2\text{-}TGF\beta_{\text{act}}]_c}_{\text{Dissociation and phosphorylation of SMAD2/3}} \quad \text{(S20)}$$

$$[SMAD3\text{-}ALK5\dot{\text{-}}R2\text{-}TGF\beta_{\text{act}}]_c = \underbrace{k_{\text{sma4a}}[SMAD3]_c[ALK5\text{-}R2\text{-}TGF\beta_{\text{act}}]_c}_{\text{Receptor complex binds to SMAD2/3}}$$
$$- \underbrace{(k_{\text{sma4b}} + k_{\text{sma5}})[SMAD3\text{-}ALK5\text{-}R2\text{-}TGF\beta_{\text{act}}]_c}_{\text{Dissociation and phosphorylation of SMAD2/3}} \quad \text{(S21)}$$

$$[pSMAD2\dot{\text{-}}SMAD4]_c = \underbrace{k_{\text{sma6a}}[SMAD4]_c[pSMAD2]_c}_{\text{pSMAD2/3 binds to SMAD4}}$$
$$- \underbrace{k_{\text{sma6b}}[pSMAD2\text{-}SMAD4]_c}_{\text{pSMAD2/3 unbinds from SMAD4}} - \underbrace{k_{\text{sma7}}[pSMAD2\text{-}SMAD4]_c}_{\text{pSMAD2/3-4 complex translocates into nucleus}} \quad \text{(S22)}$$

$$[pSMAD3\text{-}\dot{S}MAD4]_c = \underbrace{k_{\text{sma6a}}[SMAD4]_c[pSMAD3]_c}_{\text{pSMAD2/3 binds to SMAD4}} - \underbrace{k_{\text{sma6b}}[pSMAD2\text{-}SMAD4]_c}_{\text{pSMAD2/3 unbinds from SMAD4}} - \underbrace{k_{\text{sma7}}[pSMAD3\text{-}SMAD4]_c}_{\text{pSMAD2/3-4 complex translocates into nucleus}} \tag{S23}$$

$$[pSMAD2\text{-}\dot{S}MAD4]_n = \underbrace{k_{\text{sma18a}}[pSMAD2]_n[SMAD4]_n}_{\text{Nuclear pSMAD2/3 binds to SMAD4}} + \underbrace{k_{\text{sma7}}[pSMAD2\text{-}SMAD4]_c}_{\text{Translocation into nucleus}} - \underbrace{k_{\text{sma8}}[pSMAD2\text{-}SMAD4]_n}_{\text{Dephosphorylation of pSMAD2/3-4 complex}} - \underbrace{k_{\text{sma18b}}[pSMAD2\text{-}SMAD4]_n}_{\text{Nuclear complex breaks}} \tag{S24}$$

$$[pSMAD3\text{-}\dot{S}MAD4]_n = \underbrace{k_{\text{sma18a}}[pSMAD3]_n[SMAD4]_n}_{\text{Nuclear pSMAD2/3 binds to SMAD4}} + \underbrace{k_{\text{sma7}}[pSMAD3\text{-}SMAD4]_c}_{\text{Translocation into nucleus}} - \underbrace{k_{\text{sma8}}[pSMAD3\text{-}SMAD4]_n}_{\text{Dephosphorylation of pSMAD2/3-4 complex}} - \underbrace{k_{\text{sma18b}}[pSMAD3\text{-}SMAD4]_n}_{\text{Nuclear complex breaks}} \tag{S25}$$

$$[SMAD2\text{-}\dot{S}MAD4]_n = \underbrace{k_{\text{sma8}}[pSMAD2\text{-}SMAD4]_n}_{\text{Dephosphorylation}} - \underbrace{k_{\text{sma9}}[SMAD2\text{-}SMAD4]_n}_{\text{SMAD2/3-4 complex breaks}} \tag{S26}$$

$$[SMAD3\text{-}\dot{S}MAD4]_n = \underbrace{k_{\text{sma8}}[pSMAD3\text{-}SMAD4]_n}_{\text{Dephosphorylation}} - \underbrace{k_{\text{sma9}}[SMAD3\text{-}SMAD4]_n}_{\text{SMAD2/3-4 complex breaks}} \tag{S27}$$

$$[S\dot{M}AD2]_n = \underbrace{k_{\text{sma19}}[pSMAD2]_n}_{\text{Dephosphorylation}} + \underbrace{k_{\text{sma9}}[SMAD2\text{-}SMAD4]_n}_{\text{Complex breaks}} + \underbrace{k_{\text{sma10a}}[SMAD2]_c}_{\text{Translocation into nucleus}} - \underbrace{k_{\text{sma10b}}[SMAD2]_n}_{\text{Translocation out of nucleus}} \tag{S28}$$

$$[S\dot{M}AD3]_n = \underbrace{k_{\text{sma19}}[pSMAD3]_n}_{\text{Dephosphorylation}} + \underbrace{k_{\text{sma9}}[SMAD3\text{-}SMAD4]_n}_{\text{Complex breaks}} + \underbrace{k_{\text{sma10a}}[SMAD3]_c}_{\text{Translocation into nucleus}} - \underbrace{k_{\text{sma10b}}[SMAD3]_n}_{\text{Translocation out of nucleus}} \tag{S29}$$

$$[S\dot{M}AD4]_n = \underbrace{k_{\text{sma9}}([SMAD2\text{-}SMAD4]_n + [SMAD3\text{-}SMAD4]_n)}_{\text{Complex breaks}} + \underbrace{k_{\text{sma18b}}([pSMAD2\text{-}SMAD4]_n + [pSMAD3\text{-}SMAD4]_n)}_{\text{Nuclear complex breaks}} + \underbrace{k_{\text{sma11a}}[SMAD4]_c}_{\text{SMAD4 translocates into nucleus}} - \underbrace{k_{\text{sma11b}}[SMAD4]_n}_{\text{SMAD4 translocates out of nucleus}} - \underbrace{k_{\text{sma18a}}([pSMAD2]_n + [pSMAD3]_n)[SMAD4]_n}_{\text{Nuclear pSMAD2/3 binds to SMAD4}} \tag{S30}$$

$$[pS\dot{M}AD2]_n = \underbrace{k_{\text{sma17}}[pSMAD2]_c}_{\text{Translocation into nucleus}} + \underbrace{k_{\text{sma18b}}[pSMAD2\text{-}SMAD4]_n}_{\text{Complex breaks}} - \underbrace{k_{\text{sma18a}}[pSMAD2]_n[SMAD4]_n}_{\text{Binding to SMAD4}} - \underbrace{k_{\text{sma19}}[pSMAD2]_n}_{\text{Dephosphorylation}} - \underbrace{k_{\text{sma20}}[pSMAD2]_n}_{\text{Degradation}} \tag{S31}$$

$$[\dot{pSMAD3}]_n = \underbrace{k_{\text{sma17}}[pSMAD3]_c}_{\text{Translocation into nucleus}} + \underbrace{k_{\text{sma18b}}[pSMAD3\text{-}SMAD4]_n}_{\text{Complex breaks}} - \underbrace{k_{\text{sma18a}}[pSMAD3]_n[SMAD4]_n}_{\text{Binding to SMAD4}} - \underbrace{k_{\text{sma19}}[pSMAD3]_n}_{\text{Dephosphorylation}} - \underbrace{k_{\text{sma20}}[pSMAD3]_n}_{\text{Degradation}} \quad \text{(S32)}$$

$$[\dot{pSMAD3}_{\text{inh}}]_c = \underbrace{k_{\text{sma24}}[PKG_{\text{act}}][SMAD3]_c}_{\text{PKG inhibits SMAD3 via hyperphosphorylation}} - \underbrace{k_{\text{sma25}}[pSMAD3_{\text{inh}}]_c}_{\text{Cytosolic inhibited pSMAD3 desphosphorylates}} \quad \text{(S33)}$$

$$\dot{Ca} = \underbrace{k_{\text{sma26}}[pSMAD3\text{-}SMAD4]_n}_{\text{pSMAD3–4 transcription of calcific genes}} + \underbrace{k_{\text{sma27}}[pSMAD2\text{-}SMAD4]_n}_{\text{pSMAD2–4 transcription of calcific genes}} \quad \text{(S34)}$$

$$[\dot{NO}] = \underbrace{k_{\text{NO}}(\tau)}_{\text{Flow-induced NO production}} + \underbrace{k_{\text{inh1b}}[NO\text{-}sGC]}_{\text{NO unbinds from sGC}} - \underbrace{k_{\text{inh8}}[NO]}_{\text{NO degraded}} - \underbrace{k_{\text{inh1a}}[NO][sGC]}_{\text{NO binds to sGC}} \quad \text{(S35)}$$

$$[NO\text{-}\dot{s}GC] = \underbrace{k_{\text{inh1a}}[NO][sGC]}_{\text{NO binds sGC}} + \underbrace{(k_{\text{inh3b}} + k_{\text{inh5}})[NO\text{-}sGC\text{-}GTP]}_{\text{GTP unbinds or cGMP made}} - \underbrace{k_{\text{inh1b}}[NO\text{-}sGC]}_{\text{NO unbinds from sGC}} - \underbrace{k_{\text{inh3a}}[GTP][NO\text{-}sGC]}_{\text{GTP binds NO–sGC complex}} \quad \text{(S36)}$$

$$[NO\text{-}s\dot{G}C\text{-}GTP] = \underbrace{k_{\text{inh3a}}[GTP][NO\text{-}sGC]}_{\text{GTP binds NO–sGC complex}} - \underbrace{(k_{\text{inh3b}} + k_{\text{inh5}})[NO\text{-}sGC\text{-}GTP]}_{\text{GTP unbinds or cGMP made}} \quad \text{(S37)}$$

$$[s\dot{G}C] = \underbrace{(k_{\text{inh4}} + k_{\text{inh2b}})[sGC\text{-}GTP]}_{\text{GTP unbinds or cGMP made}} + \underbrace{k_{\text{inh1b}}[NO\text{-}sGC]}_{\text{NO unbinds from sGC}} - \underbrace{k_{\text{inh2a}}[sGC][GTP]}_{\text{GTP binds sGC}} - \underbrace{k_{\text{inh1a}}[NO][sGC]}_{\text{NO binds sGC}} \quad \text{(S38)}$$

$$[sGC\text{-}\dot{G}TP] = \underbrace{k_{\text{inh2a}}[sGC][GTP]}_{\text{GTP binds sGC}} - \underbrace{(k_{\text{inh4}} + k_{\text{inh2b}})[sGC\text{-}GTP]}_{\text{cGMP made or GTP unbinds}} \quad \text{(S39)}$$

$$[\dot{GTP}] = \underbrace{k_{\text{inh3b}}[NO\text{-}sGC\text{-}GTP]}_{\text{GTP unbinds from NO–sGC}} + \underbrace{k_{\text{inh2b}}[sGC\text{-}GTP]}_{\text{GTP unbinds from sGC}} + \underbrace{k_{\text{kinh11}}[GMP]}_{\text{GMP recycled back to GTP}} - \underbrace{k_{\text{inh2a}}[sGC][GTP]}_{\text{GTP binds sGC}} - \underbrace{k_{\text{inh3a}}[GTP][NO\text{-}sGC]}_{\text{GTP binds NO–sGC}} \quad \text{(S40)}$$

$$[c\dot{GMP}] = \underbrace{k_{\text{inh5}}[NO\text{-}sGC\text{-}GTP]}_{\text{cGMP made from NO–sGC–GTP}} + \underbrace{k_{\text{inh4}}[sGC\text{-}GTP]}_{\text{cGMP made from sGC–GTP}} + \underbrace{k_{\text{inh6b}}[PDE\text{-}cGMP]}_{\text{cGMP unbinds from PDE}} - \underbrace{k_{\text{inh6a}}[cGMP][PDE]}_{\text{cGMP binds PDE}} \quad \text{(S41)}$$

$$[PDE\text{-}\dot{c}GMP] = \underbrace{k_{\text{inh6a}}[cGMP][PDE]}_{\text{cGMP binds PDE}} - \underbrace{(k_{\text{inh7}} + k_{\text{inh6b}})[PDE\text{-}cGMP]}_{\text{GMP made or cGMP unbinds}} \quad \text{(S42)}$$

$$[\dot{GMP}] = \underbrace{k_{\text{inh7}}[PDE\text{-}cGMP]}_{\text{GMP made from cGMP–PDE complex}} - \underbrace{k_{\text{inh11}}[GMP]}_{\text{GMP recycled back to GTP}} \quad \text{(S43)}$$

$$[\dot{PDE}] = \underbrace{(k_{\text{inh7}} + k_{\text{inh6b}})[PDE\text{-}cGMP]}_{\text{PDE released from cGMP–PDE}} - \underbrace{k_{\text{inh6a}}[cGMP][PDE]}_{\text{cGMP binds PDE}} \quad \text{(S44)}$$

$$[\dot{PKG}] = \underbrace{k_{\text{inh10}}[PKG_{\text{act}}]}_{\text{PKG autoinhibitory deactivation}} - \underbrace{k_{\text{inh9}}[PKG][cGMP]}_{\text{cGMP activates PKG}} \quad \text{(S45)}$$

$$[\dot{PKG}_{\text{act}}] = \underbrace{k_{\text{inh9}}[PKG][cGMP]}_{\text{cGMP activates PKG}} - \underbrace{k_{\text{inh10}}[PKG_{\text{act}}]}_{\text{PKG deactivates}} \quad \text{(S46)}$$

Rate constant and initial species concentration values

Table S4: ***Rate constants for the inflammation pathway model.***

Parameter	Value	Definition	Reference
k_{inf1}	See Eq. (S47)	Subendothelial LDL penetration	Arzani et al.[21]
$\overline{k}_{\text{inf1}}$	3.78×10^{-6} s^{-1}	Baseline LDL penetration	Arzani et al.[21]
k_{inf2}	2.40×10^{-5} s^{-1}	LDL out diffusion	Arzani et al.[21]
k_{inf3}	3×10^{-4} s^{-1}	LDL oxidation	Arzani et al.[21]
k_{inf4}	1.71×10^{-16} M^{-1}s^{-1}	Foam cell formation	Arzani et al.[21]
k_{inf5}	See Eq. (S48)	Monocyte capture via LDL	Arzani et al.[21]
$\overline{k}_{\text{inf5}}$	6.37×10^{5} s^{-1}	Baseline monocyte capture	Arzani et al.[21]
k_{inf6}	1.15×10^{-6} s^{-1}	Monocyte $\rightarrow$ macrophage differentiation	Arzani et al.[21]
k_{inf7}	2.76×10^{-6} s^{-1}	Monocyte apoptosis	Arzani et al.[21]
k_{inf8}	7.41×10^{-13} M^{-1}s^{-1}	TGF-β activation	Arzani et al.[21]
k_{inf9}	1.22×10^{-8} s^{-1}	Foam cell apoptosis	Inferred from Jiang et al.[76] and Bajpai et al.[77]
k_{inf10}	See Eq. (S49)	Latent TGF-β production	Arzani et al.[21]
k_{inf11}	5.78×10^{-3} s^{-1}	Active TGF-β degradation	Arzani et al.[21]
k_{inf12}	1.28×10^{-4} s^{-1}	Latent TGF-β degradation	Arzani et al.[21]
k_{inf13}	1.32×10^{-9} s^{-1}	Macrophage apoptosis	Estimated from Bajpai et al.[77]

In Table S4, k_{inf1} is based on Arzani et al.,[21] who reported a baseline LDL penetration rate, which we denote as $\overline{k}_{\text{inf1}}$. This value is multiplied by a factor $(1 + \bar{\tau}/\bar{\tau}_{\text{ref}})^{-1}$ to account for the effects of WSS on LDL penetration, i.e.,

$$k_{\text{inf1}}(\tau) = \frac{\overline{k}_{inf1}}{1 + \bar{\tau}/\bar{\tau}_{\text{ref}}}. \tag{S47}$$

Similarly, k_{inf5} is based on the second-order rate constant reported by Arzani et al.[21] for the interaction between monocytes and LDL. We multiply this by the same scaling factor to account for variations in WSS, i.e.,

$$k_{\text{inf5}}(\tau) = \frac{\overline{k}_{inf5}}{1 + \bar{\tau}/\bar{\tau}_{\text{ref}}}. \tag{S48}$$

Additionally, we define the rate constant for foam cell apoptosis as $k_{\text{inf9}} = 9.28 \cdot k_{\text{inf13}}$, where k_{inf13} is the macrophage apoptosis rate constant. This is based on results from Bajpai et al.,[77] who estimated the percentage of sex-mismatched CCR2^{+} macrophages in the body after 8.8 years. They also reported that oxLDL-treated macrophages had a 47.7% apoptosis rate after 48h, compared to 5.14% in control, which is a ∼9.28-fold increase in the apoptosis rate for foam cells.

Finally, the rate constant for latent TGF-β production, k_{inf10}, is assumed to depend on the total concentration of immune cells ([*Foam Cell*]+[*Macrophage*]) and V_{valve} (Table 1), which assumes different values depending on valve thickness,

$$k_{\text{inf10}} = \alpha \cdot \frac{3.3 \times 10^{-7} \cdot ([\textit{Foam Cell}] + [\textit{Macrophage}]) \cdot V_{\text{valve}}}{\alpha \cdot ([\textit{Foam Cell}] + [\textit{Macrophage}]) \cdot V_{\text{valve}} \cdot \psi + 2.84 \times 10^{4}}. \tag{S49}$$

Here, α is the foam cell formation ratio (see Table 1) and ψ is a unit conversion factor defined as *Desired units* = *Current units*/ψ. In Arzani et al.,[21] immune cell concentrations are in g/m^3 and V_{valve} is in m^3. This gives k_{inf10} in units of g/(s·m^3). The conversion factor ψ is used here to convert k_{inf10} into units of M/s, consistent with the other sub-models in the SB model.

Table S5: ***Rate constants for the NO regulation model.***

Parameter	Value	Definition	Reference
k_{inh1a}	0.78×10^6 $\text{M}^{-1}\text{s}^{-1}$	NO binds to sGC	Inferred from Sharina and Martin[78]
k_{inh1b}	1.8×10^{-1} s^{-1}	NO unbinds from sGC	Sayed et al.[79]
k_{inh2a}	2.5×10^5 $\text{M}^{-1}\text{s}^{-1}$	GTP binds to sGC	*See text below*
k_{inh2b}	1.8×10^2 s^{-1}	GTP unbinds from sGC	Garmaroudi et al.[29]
k_{inh3a}	3.13×10^7 $\text{M}^{-1}\text{s}^{-1}$	GTP binds to NO-sGC	*See text below*
k_{inh3b}	4.3×10 s^{-1}	GTP unbinds from NO-sGC	Garmaroudi et al.[29]
k_{inh4}	1.5×10^{-1} s^{-1}	cGMP made from GTP-sGC	Garmaroudi et al.[29]
k_{inh5}	2.87×10 s^{-1}	cGMP made from NO-GTP-sGC	Garmaroudi et al.[29]
k_{inh6a}	3.13×10^8 $\text{M}^{-1}\text{s}^{-1}$	cGMP binds to PDE	Garmaroudi et al.[29]
k_{inh6b}	1.30×10^{-1} s^{-1}	cGMP unbinds from PDE	Garmaroudi et al.[29]
k_{inh7}	2.2 s^{-1}	GMP made from cGMP-PDE	Garmaroudi et al.[29]
k_{inh8}	1.4 s^{-1}	NO degradation	Thomas et al.[80]
k_{inh9}	3.13×10^4 $\text{M}^{-1}\text{s}^{-1}$	cGMP activates PKG	*See text below*
k_{inh10}	5×10^{-3} s^{-1}	PKG autoinhibitory deactivation	Inferred from Srihirun et al.[81]
k_{inh11}	1.5×10^{-3} s^{-1}	GMP recycled back to GTP	Inferred from Khan et al.[82] and Mckee et al.[83]

In Table S5, the rate constant for NO–sGC binding, k_{inh1a} is based on the intrinsic cellular association rate constant $k_{\text{on}} = 1.4\text{–}4.5 \times 10^8$ $\text{M}^{-1}\text{s}^{-1}$, reported by Sharina et al.[78] Because sGC-expressing cells occupy less volume than the full leaflet, by roughly two orders of magnitude, most NO molecules diffuse without encountering the enzyme. Following the homogenization framework of Nicholson and Bassingthwaighte,[84,85] we scale k_{on} by this volumetric factor to obtain an effective tissue-level rate constant $k_{\text{eff}} \approx 0.45\text{–}1.44 \times 10^6$ $\text{M}^{-1}\text{s}^{-1}$. Based on this, we set $k_{\text{inh1a}} = 0.78 \times 10^6$ $\text{M}^{-1}\text{s}^{-1}$.

For k_{inh3a}, the rate constant for GTP binding to the NO–sGC complex, we adopted a tissue-level rate corresponding to a cellular value of $\sim 10^5$ $\text{M}^{-1}\text{s}^{-1}$. The use of a lower effective rate is intentional: k_{inh3a} is treated as a phenomenological parameter that captures system-level constraints, such as spatial hindrance, allosteric effects, or post-translational modifications, which may reduce the efficiency of GTP association with NO-bound sGC *in vivo*. A similar rationale is used for k_{inh2a}, which describes GTP binding to inactive sGC. Here, we set $k_{\text{inh2a}} < k_{\text{inh3a}}$, consistent with reports that NO binding induces a conformational change that increases the affinity of sGC for GTP. By encoding this mechanistic asymmetry, rather than assuming equal binding rates,[29] the model more faithfully represents the sequential activation and catalytic behavior of sGC.

For k_{inh9}, although cGMP binds PKG rapidly *in vitro*, we again employ a lower effective rate constant to represent macroscopic factors such as intracellular buffering, compartmentalization, and cooperative activation. The calibrated value yields physiologically reasonable PKG dynamics. For the PKG deactivation rate constant k_{inh10}, we selected a conservative value of 5×10^{-3} s^{-1} based on work by Srihirun et al.,[81] who reported a peak in the PKG activity marker P-VASP Ser239 at approximately 15 min, follwed by a return to baseline by 60 min. Fitting an exponential decay to a 5% residual yields $t_{1/2} \approx 10.4$ min ($k \approx 1.1 \times 10^{-3}$ s^{-1}). However, since the signal may have fully decayed, or simply fallen below the $\sim 5\%$ noise floor, we adopt $k = 5 \times 10^{-3}$ s^{-1} to ensure complete deactivation within the observed experimental window.

Finally, the rate constant for GMP $\rightarrow$ GTP recycling, k_{inh11}, was chosen to lie between experimentally grounded lower and upper bounds. A lower bound of $\sim 7.7 \times 10^{-5}$ s^{-1} was inferred from McKee et al.,[83] who observed 13% guanine nucleotide conversion over 30 min in isolated cardiac mitochondria. As an upper bound, we computed an effective first-order rate constant, $k_{\text{inh11}}^{\text{upper}} = k_{\text{cat}}[E]/K_M$, from Michaelis–Menten kinetics (assuming $[\text{GMP}] \ll K_M$) using parameters from Figure 6E of Khan et al.[82] and an enzyme concentration of

10 nM, matching their assays. The resulting values spanned 0.015–0.045 s^{-1} across six variants. Because this study characterized only GMP → GDP conversion and the assumption [GMP] $\ll K_M$ may fail as GMP accumulates, the true physiological rate likely falls below this range. Thus, our choice of 1.5×10^{-3} s^{-1} represents a conservative, physiologically plausible estimate.

Table S6: ***Rate constants for the SMAD signaling pathway model***

Parameter	Value	Description	Reference
k_{sma1a}	4.14×10^{10} $M^{-1}s^{-1}$	TGF-β binds to R2 receptor	Chung et al.[33]
k_{sma1b}	4.97×10^{-3} s^{-1}	TGF-β unbinds from R2 receptor	Chung et al.[33]
k_{sma2a}	4.14×10^{10} $M^{-1}s^{-1}$	Receptor complex formation with ALK5	Chung et al.[33]
k_{sma2b}	4.97×10^{-3} s^{-1}	ALK5 dissociates from receptor complex	Chung et al.[33]
k_{sma3}	6.58×10^{-3} s^{-1}	Receptor complex detaches from the cell surface	Chung et al.[33]
k_{sma4a}	9.42×10^{8} $M^{-1}s^{-1}$	Receptor complex binds to SMAD2/3	Chung et al.[33]
k_{sma4b}	1.62×10^{-2} s^{-1}	Receptor complex dissociates from SMAD2/3	Chung et al.[33]
k_{sma5}	7.47×10^{2} s^{-1}	Receptor complex phosphorylates SMAD2/3	Chung et al.[33]
k_{sma6a}	3.77×10^{10} $M^{-1}s^{-1}$	pSMAD2/3 binds to SMAD4 to form pSMAD2/3-4	Chung et al.[33]
k_{sma6b}	2.43×10^{1} s^{-1}	pSMAD2/3 unbinds from SMAD4	Chung et al.[33]
k_{sma7}	1.35×10^{-2} s^{-1}	pSMAD2/3-4 complex translocates into nucleus	Chung et al.[33]
k_{sma8}	4.2×10^{-4} s^{-1}	pSMAD2/3-4 complex dephosphorylates	Chung et al.[33]
k_{sma9}	1.68×10^{-3} s^{-1}	SMAD2/3-4 complex breaks	Chung et al.[33]
k_{sma10a}	2.7×10^{-3} s^{-1}	SMAD2/3 translocates into nucleus	Chung et al.[33]
k_{sma10b}	5.8×10^{-3} s^{-1}	SMAD2/3 translocates out of nucleus	Chung et al.[33]
k_{sma11a}	3.35×10^{-4} s^{-1}	SMAD4 translocates into nucleus	Chung et al.[33]
k_{sma11b}	2.9×10^{-3} s^{-1}	SMAD4 translocates out of nucleus	Chung et al.[33]
k_{sma12a}	3.54×10^{-16} $M^{-1}s^{-1}$	R2 receptor synthesis	Chung et al.[33]
k_{sma12b}	4.67×10^{-4} s^{-1}	R2 receptor degradation	Chung et al.[33]
k_{sma13a}	3.54×10^{-16} $M^{-1}s^{-1}$	ALK5 receptor synthesis	Chung et al.[33]
k_{sma13b}	4.67×10^{-4} s^{-1}	ALK5 receptor degredation	Chung et al.[33]
k_{sma14a}	1.21×10^{-15} $M^{-1}s^{-1}$	SMAD2/3 synthesis	Chung et al.[33]
k_{sma14b}	1.08×10^{-5} s^{-1}	SMAD2/3 degredation	Chung et al.[33]
k_{sma15a}	2.21×10^{-15} $M^{-1}s^{-1}$	SMAD4 synthesis	Chung et al.[33]
k_{sma15b}	2×10^{-5} s^{-1}	SMAD4 degredation	Chung et al.[33]
k_{sma16ld}	6.58×10^{-3} s^{-1}	Ligand induced degradation of receptor complex	Chung et al.[33]
k_{sma16cd}	4.67×10^{-4} s^{-1}	Constitutive degradation of receptor complex	Chung et al.[33]
k_{sma17}	8.38×10^{-3} s^{-1}	pSMAD2/3 translocates into nucleus	Chung et al.[33]
k_{sma18a}	1.05×10^{9} $M^{-1}s^{-1}$	Nuclear pSMAD2/3 binds to SMAD4	Chung et al.[33]
k_{sma18b}	1.52×10^{-2} s^{-1}	Nuclear pSMAD2/3-4 complex breaks	Chung et al.[33]
k_{sma19}	4.2×10^{-4} s^{-1}	Nuclear pSMAD2/3 dephosphorylates	Chung et al.[33]
k_{sma20}	9×10^{-5} s^{-1}	Nuclear SMAD2/3 degradation	Chung et al.[33]
k_{sma21a}	6.58×10^{-3} s^{-1}	R2 receptor goes into cytoplasm	Chung et al.[33]
k_{sma21b}	6.58×10^{-4} s^{-1}	R2 receptor reattaches to surface	Chung et al.[33]
k_{sma22a}	6.58×10^{-3} s^{-1}	ALK5 receptor goes into cytoplasm	Chung et al.[33]
k_{sma22b}	6.58×10^{-4} s^{-1}	ALK5 receptor reattaches to surface	Chung et al.[33]
k_{sma23}	6.58×10^{-4} s^{-1}	Receptor complex breaks completely	Chung et al.[33]
k_{sma24}	5×10^{3} $M^{-1}s^{-1}$	PKG inhibits SMAD3 via hyperphosphorylation	Chung et al.[33]
k_{sma25}	4.20×10^{-4} s^{-1}	Cytosolic inhibited pSMAD3 desphosphorylates	Chung et al.[33]
k_{sma26}	See Eq. (20)	pSMAD3-4 transcribes pro-calcific genes	N/A
k_{sma27}	See Eq. (21)	pSMAD2-4 transcribes pro-calcific genes	N/A

Table S7: ***Initial concentrations for the integrated SB model.***

Species	Initial Amount (M)	Reference
LDL	0	Arzani et al.[21]
oxLDL	0	Arzani et al.[21]
Monocytes	0	Arzani et al.[21]
Macrophages	0	Arzani et al.[21]
Foam Cells	0	Arzani et al.[21]
TGF-β	0	Arzani et al.[21]
TGF-β_{act}	0	Arzani et al.[21]
NO	3.84×10^{-11}	He and Liu[86]
ALK5$_c$	1.19×10^{-11}	Chung et al.[33]
ALK5$_s$	1.33×10^{-12}	Chung et al.[33]
R2$_c$	1.19×10^{-11}	Chung et al.[33]
R2$_s$	1.33×10^{-12}	Chung et al.[33]
Smad2$_c$	2.26×10^{-10}	Chung et al.[33]
Smad2$_n$	3.98×10^{-11}	Chung et al.[33]
Smad3$_c$	2.26×10^{-10}	Chung et al.[33]
Smad3$_n$	3.98×10^{-11}	Chung et al.[33]
Smad4$_c$	3.31×10^{-10}	Chung et al.[33]
Smad4$_n$	3.45×10^{-11}	Chung et al.[33]
sGC	3.2×10^{-10}	Garmaroudi et al.[29]
GTP	9.75×10^{-7}	Garmaroudi et al.[29]
cGMP	0	Garmaroudi et al.[29]
PDE	4.8×10^{-10}	Garmaroudi et al.[29]
PKG	3.2×10^{-8}	Inferred from Keilbach et al.[87]
PKG$_{\text{act}}$	0	N/A

In Table S7, the initial concentrations of PKG and PKG$_{\text{act}}$ are based on estimates from Keilbach et al.,[87] who reported tissue concentrations for PKG of ∼10 pmol/g of wet tissue. Assuming a tissue density of 1 g/mL, this corresponds to a tissue concentration on the order of 10^{-8} M. Because the reported values in the study were somewhat higher, we adopt this estimate as the total PKG concentration and set the initial concentration of PKG accordingly. The active form, PKG_{act}, is initialized at 0.

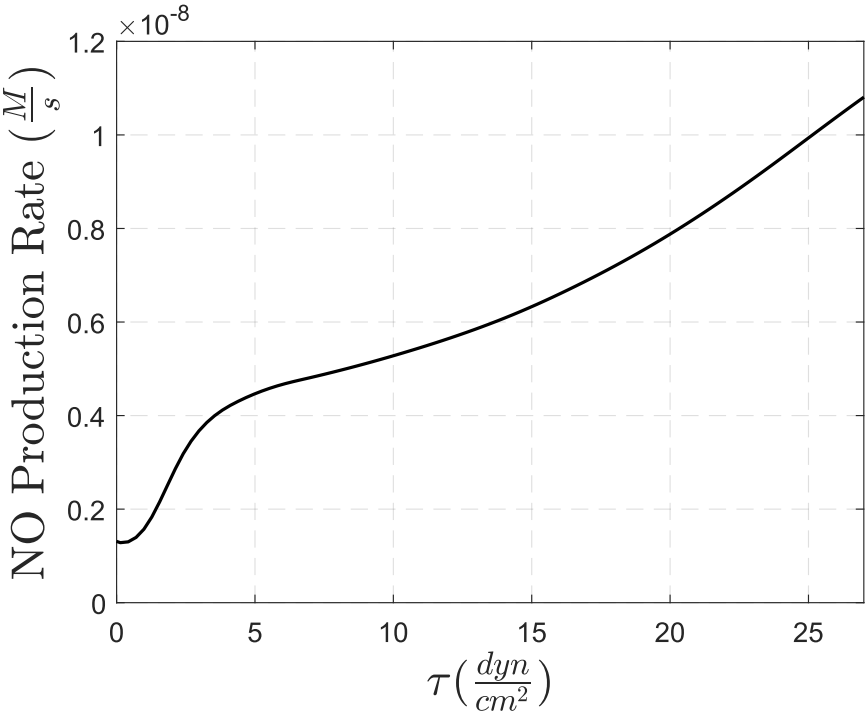

Figure S1: *NO production rate (in M/s) vs. shear stress (in dynes per* cm^2*). Taken from Sriram et al.*[36]